The Electron Hole System in Two-Dimensional Semiconductors and Their Heterostructures

Jue Wang

Submitted in partial fulfillment of the
requirements for the degree of
Doctor of Philosophy
in the Graduate School of Arts and Sciences

COLUMBIA UNIVERSITY

2020

Abstract

The Electron Hole System in Two-Dimensional Semiconductors and Their Heterostructures

Jue Wang

The discovery of two-dimensional (2D) transition metal dichalcogenides (TMDCs), a new group of direct band gap semiconductors, and their heterostructures, provides unprecedented opportunities to the research and application of exciton and related species. The strong Coulomb interaction in those materials correlated the photo-excited electron hole system and generates series of exotic electronic phases. In this dissertation, I will focus on two of such systems: the interlayer exciton in TMDC heterobilayers and the trion in TMDC monolayers.

With the first generation TMDC samples, the carrier dynamics in MoS_2/WSe_2 heterobilayers was studied as a function of twist angle. The twist angle independence of the ultrafast charge transfer indicates a hot carrier mediated charge transfer mechanism, while that of charge recombination was attributed to defect-mediated non-radiative charge recombination. The development of second generation TMDC samples, characterized by BN encapsulation and flux growth of bulk crystals, facilitates the revelation of intrinsic properties of those materials.

In $MoSe_2/WSe_2$ heterobilayers, the Mott transition from insulating interlayer exciton to conducting charge separated electron/hole plasmas was investigated by photoluminescence, transient reflectance, photoconductivity and diffusion measurements and directly observed in time and space. The high carrier density of more than 10^{14} cm^{-2} can be optically generated under both continuous wave and pulsed excitation conditions. This work paves the way towards predicted high-temperature exciton condensate in TMDC heterostructures.

In $MoSe_2$ monolayers, the nature of trion was revealed by time and energy resolved photoluminescence imaging. The trion binding energy is exceptionally tolerant to dielectric disorder, the temperature dependence of which disfavors the virtual trion theory. The higher diffusion constant of trion than exciton supports that it is a mobile charged species in contradiction to the exciton polaron theory. The trionic resonance is robust against Mott transition leading to the trionic emission and the ring diffusion pattern at high excitation densities. Our observations demonstrate that the trion in monolayer $MoSe_2$ is a robust and mobile carrier of charge and energy.

Table of Contents

List of Figures

Acknowledgements

It is my great pleasure to thank all those people who contributed to this dissertation. Professor Xiaoyang Zhu (aka. X.-Y. Zhu or XYZ), my doctoral advisor, deserves most of the credit. During my doctoral study, Professor Zhu has provided me with full freedom to explore new problems, complete trust in developing new techniques, key insights in interpreting data and narrating stories, valuable suggestions on being a scientist as well as adequate funding to support my concentration in science. Professor Zhu has led me into the fields of condensed matter physics and spectroscopy and shaped my taste of science; His approval of my intellectual competence in science will always encourage me in pursuing truth.

Secondly, I would like to acknowledge the whole XYZ group, a big family of which I feel very fortunate to be a member for the past five years, including Dr. Cory Nelson, Dr. Xiaoxi Wu, Dr. Timothy Atallah, Dr. Kris Williams, Dr. Tyler Evans, Dr. Xinjue Zhong, Dr. Kihong Lee, Dr. Prakriti Joshi, Andrew Schlaus, Michael Spencer, Felisa Conrad-Burton, Yufeng Liu and Prof. Haiming Zhu, Prof. Kiyoshi Miyata, Dr. Daniel Niesner, Dr. Martin Gustafsson, Dr. M. Tuan Trinh, Dr. Fang Liu, Dr. Florian Geyer, Dr. Feifan Wang, Dr. Sebastian Maehrlein, Dr. Yusong Bai, Dr. Mark Ziffer, Dr. Doyk Hwang, Dr. Yanan Dai, Dr. Qiuyang Li, Dr. Yongping Fu, Dr. Lucas Huber as well as Prof. Lin Zhou, Dr. James Gong, Wenjing Wu, Bryan Kudisch, Osman Moneer and Neyanel Vasquez. To me, the XYZ group is not only a close-knit and vibrant scientific community where I can learn all aspects of science from different people but also a model cross-cultural communication school that has bridged the gap between me and the English-speaking world.

In particular, I would like to thank Prof. Haiming Zhu whom I shadowed in my second year for introducing me to the ultrafast spectroscopy and microscopy of semiconductors and demonstrating his high efficiency in achieving academic success; Prof. Kiyoshi Miyata for answering all my scientific and technical questions in my third and fourth year, especially his help in setting up the spectrally resolved pump-probe spectroscopy, and manifesting his erudition and modesty; Dr. Yusong Bai for our fruitful collaboration in my fifth year and for reminding me of the cruelty of academia; and Dr. Timothy Atallah for being the go-to person for all the subtleties of the lab.

This dissertation would not be possible without the support of Columbia's 2D materials synthesis and fabrication team, led by Prof. James Hone. I am particularly indebted to Dr. Jenny Ardelean and Prof. Lin Zhou who made the major heterostructures used in this dissertation; I would also like to express my gratitude to everyone for their hard work in our sample team which includes Wenjing Wu, Dr. James Gong, Young Duck Kim, Osman Moneer and Neyanel Vasquez. Thanks to Prof. Daniel Rhodes, Bumho Kim and Dr. Song Liu for providing high-quality flux TMDC crystals and Dr. Takashi Taniguchi and Dr. Kenji Watanabe for providing h-BN crystals.

I would like to thank our collaborators, Prof. Mack Kira, Prof. Frank Jahnke, Dr. Alexander Steinhoff and Dr. Matthias Florian for their theoretical support in understanding the optical response of heterostructures; Prof. Xiaodong Xu, Dr. Pasqual Rivera and Nathan Wilson for perceptive discussions and sharing precious samples; Prof. Cory Dean, Dr. Qianhui Shi and En-Min Shih for their support on electronic device fabrication and measurements; and Hanqing Xiong for his considerable assistance in building the scanning confocal microscope. I would like to acknowledge Gary Eisenmann from Coherent, Inc. for his help in maintaining our ultrafast

laser and Kerry Neal from Montana Instruments for her help in the initial setup of the helium cryostation. In addition, Prof. Kenneth Eisenthal and Prof. Louis Brus were kind enough to offer us their lab space and optics which were used in this dissertation.

I would like to record my appreciation to Prof. David Reichman, Prof. Wei Min, Prof. James Hone and Prof. Louis Brus for serving my dissertation defense committee and giving constructive suggestions; Special thanks to Prof. Reichman and Prof. Min for serving my advisory committee and always thinking highly of me in the past five years.

Finally, I thank my parents, Xiaomei and Yanyi Wang, for wholeheartedly supporting me in becoming a scientist and forgiving me for not going home for years. Thanks to my lovely girlfriend, Yiqiu Liu, for her daily encouragement and annual vacation plans since the first day of my graduate life that has been invaluable to me in surviving the academia.

Jue Wang

December 2019, New York

This page intentionally left blank

To Yiqiu Liu

This page intentionally left blank

Chapter 1

Introduction

This chapter introduces the electron-hole system in photo-excited two-dimensional (2D) semiconductors and their heterostructures. The strong Coulomb interaction correlates photo-excited electrons and holes and generates a series of electronic phases in those systems. In particular, 1.1, 1.2 and 1.3 are devoted to the electron-hole system in photo-excited 2D semiconductors at different carrier densities, i.e. excitons in the low density regime (1.1), exciton complexes in the intermediate density regime (1.2) and electron-hole plasma in the high density regime (1.3); 1.4 focuses on interlayer excitons in photo-excited 2D semiconductor heterostructures. In the context of extensive research in literature, the scope of this dissertation is stated in 1.5.

1.1 Excitons in 2D semiconductors

Atomically thin transition metal dichalcogenides (TMDCs) are direct band gap semiconductors[1] with formula MX_2 (M = Mo, W, X = S, Se). Its 2D hexagonal lattice is similar to graphene while the two carbon atoms in a unit cell are substituted by one M atom and two X atoms above and below the 2D plane formed by M. This section serves as a brief summary of the rich exciton physics in 2D TMDCs. Interested reader are referred to detailed reviews[2,3].

In the band structure of TMDCs, the valance band maximum (VBM) and conduction band minimum (CBM) are located at the energetically degenerate but inequivalent corners of the hexagonal Brillouin zone, i.e. K and -K points. First principles calculations show that the d orbitals of M and p orbitals of X are the primary contributors to the bands near the band gap[3]. In

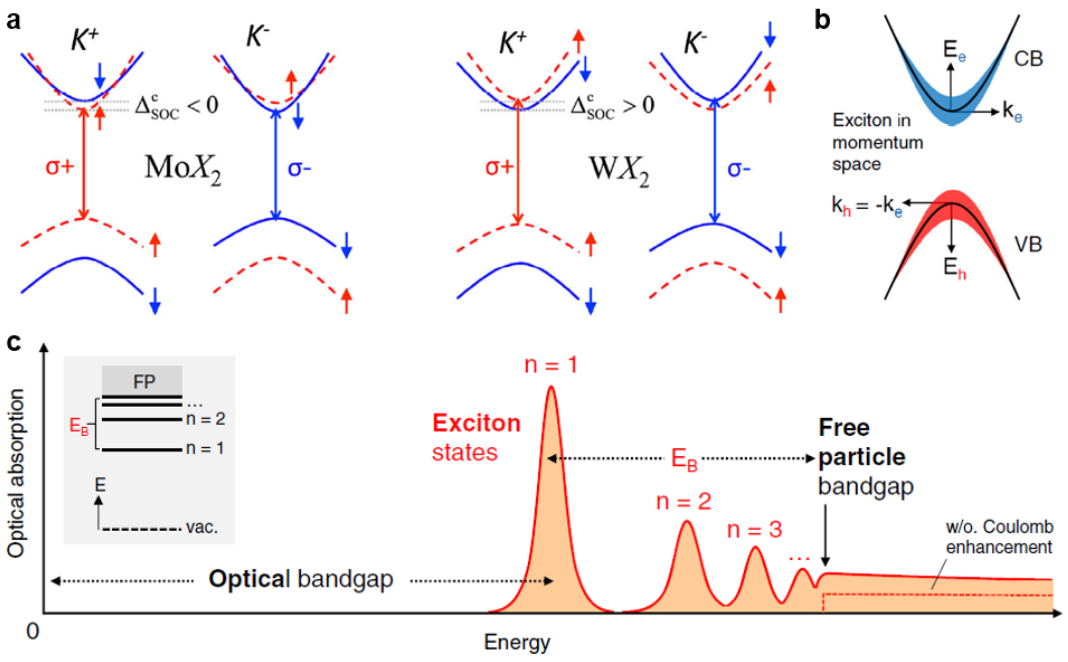

Figure 1.1 | Excitons in TMDCs. a, Valley optical selection rule and spin orbit coupling in MoX_2 and WX_2. **b**, Composition of exciton in reciprocal space. **c**, optical response of TMDCs. Panels **a**, **b** and **c** adapted from ref. [2], American Physical Society.

contrast to the band edge states at ±K points which are majorly from metal d orbitals, the conduction band (CB) at Q and the valance band (VB) at Γ has significant contributions from p_z orbitals of X, whose interlayer hopping lead to the direct-indirect transition from monolayer to bulk[4].

The carriers at the band extrema (valleys) acquire an additional quantum number, i.e. valley index or pseudospin. The C_{3h} point group symmetry, especially the lack of inversion symmetry, at ±K points result in a chiral optical selection rule, i.e. the optical transitions at K (-K) valleys are allowed only with σ+ (σ-) polarized light[5,6]. Therefore, circularly polarized light can selectively excite excitons in one of the ±K valleys, while linearly polarized light can be used to create valley coherence between the ±K valleys.

The inclusion of heavy atoms and the involvement of metal d orbitals give rise to the strong spin-orbit coupling (SOC) in TMDCs. The VB spin splitting at ±K valleys is about 0.2 eV (M = Mo) or 0.4 eV (M = W) and the CB spin splitting is a few (MoS_2) to tens of meV[2]. The excitons associated with spin split band extrema are therefore energetically separated by hundreds of meV, termed A and B excitons. The mirror reflection symmetry allows only out-of-plane spin; the time inversion symmetry dictates that the SOC at ±K valleys to have the same amplitude but different sign. Therefore, the valley polarized excitons are also spin polarized, i.e. spin-valley locking[3]. Furthermore, Mo and W based TMDCs have different signs of SOC, making lowest energy excitons in WX_2 spin-forbidden (dark excitons)[2].

In addition to valley optical selection rule, spin-orbit coupling and valley-spin locking effects, the TMDCs as semiconductors feature exceptionally strong Coulomb interaction with a typical exciton binding energy of 0.5 eV[2]. It is a combined effect of extreme quantum confinement, large effective mass (~0.5m_0 for both electron and hole[7,8]) and small dielectric screening effect from the environment[2]. This can be seen from the binding energy of a 2D exciton in 3D Coulomb potential[9]:

$$E_{\mathrm{B}} = \frac{\mu}{m_0 \varepsilon^2 \left(n - \frac{1}{2} \right)^2} \mathrm{Ry}$$

$E_{\mathrm{B}} \approx 0.5$ eV is obtained with reduced exciton mass $\mu = \frac{m_{\mathrm{e}} m_{\mathrm{h}}}{m_{\mathrm{e}} + m_{\mathrm{h}}} \approx 0.25 m_0$, effective dielectric constant of BN $\varepsilon \approx 5$ and Rydberg constant $\mathrm{Ry} \approx 13.6$ eV. The exciton Bohr radius[9] $a_{\mathrm{B}} \propto \frac{\varepsilon}{\mu}\left(n - \frac{1}{2} \right)$ is relatively small (~1 nm)[2] but still well-described by Wannier-Mott theory.

The large binding energy (as well as corresponding large oscillator strength) make it possible to resolve the Rydberg excitons up to n = 5 between 1s exciton and band gap[10]. The energy levels

deviate from hydrogenic model because of the anisotropic screening of Coulomb interaction[10]. Moreover, the absorption of electron-hole continuum should also be Coulomb enhanced[11].

The relative air insensitivity of TMDCs make them easy to access and handle. There are two major types of fabrication method: the top-down approach where the monolayer is obtained from scotch tape exfoliation, or micromechanical cleavage, of bulk TMDCs[1] and the bottom-up approach of chemical vapor deposition (CVD). While the CVD method is more favorable for industrial applications, currently the exfoliated samples demonstrate higher quality and are mostly used in academic research[2]. Continuous efforts have been made to improve the material quality and approach the intrinsic properties. Boron nitride (BN) encapsulation has been shown to reduce the exciton linewidth to about 2 meV, close to the 1 meV intrinsic limit, possibly by isolating the material from surface effect and chemistry with air and moisture[12]. Flux growth method has been used to synthesize high quality bulk selenides which reduce the defect density[13] of exfoliated monolayers to less than 10^{11} cm^{-2}.

1.2 Exciton complexes in 2D semiconductors

Beyond exciton, a two-body bound state, the strong Coulomb interaction can mediate many-body interaction and form more quasiparticles know as exciton complexes at finite carrier densities. An exciton can bound an electron (a hole) to form charged exciton, or negative (positive) trion, first observed in MoS_2 and $MoSe_2$ in 2013[14,15]; two excitons can bound to form a biexciton, or an exciton molecule, first observed in WSe_2 in 2015[16]; two exciton and an electron (a hole) can bound to form a charged biexciton, or negative (positive) quinton, first observed in WSe_2 in 2018[17–20]. The second generation of TMDC samples, especially the $MoSe_2$ and WSe_2 exfoliated from flux grown bulk crystals[13] and encapsulated by BN[12], show well-separated and

ultra-sharp exciton and exciton complexes peaks in photoluminescence spectrum, making it a model system to study those Coulomb correlated many-body quasiparticles.

The observed binding energy of trion is about (20~30) meV[14,15], nearly an order of magnitude larger than in conventional quantum well systems[21]. At finite doping level, the energy difference between exciton and trion includes both the trion binding energy and the Fermi level[14]:

$$E_{\mathrm{X}} - E_{\mathrm{X}^-} = E_{\mathrm{B}}^{\mathrm{X}^-} + E_{\mathrm{F}}$$

The exciton, trion and electron were shown to be in chemical equilibrium at each temperature[15]:

$$\frac{n_{\mathrm{X}} n_{\mathrm{e}^-}}{n_{\mathrm{X}^-}} = \frac{4 m_{\mathrm{e}} k_{\mathrm{B}} T}{\pi \hbar^2} \exp\left(-\frac{E_{\mathrm{B}}^{\mathrm{X}^-}}{k_{\mathrm{B}} T} \right)$$

Due to energy and momentum conservation, the recombination of a trion at finite momentum **k** will leave an electron at similar momentum but with different effective mass m_{e}, resulting in the low energy tail of trion PL (the electron recoil effect)[15]. The negative and positive trions, created by electron and hole doping respectively, have similar binding energy because of the similar effective mass of electron and hole in TMDCs[2,7,8].

While the few-body quasiparticle picture works well at relatively low carrier densities, there have been debate on the nature of those experimental observations. At a finite doping level, the absorption spectroscopy was attributed to the dressing of exciton by the Fermi sea of charge carriers forming attractive and repulsive polarons[22,23]. The similarity between trion binding energy and optical phonon energy has also raised the doubt that only virtual trion is formed when a localized electron captures an election by emitting an optical phonon[24].

1.3 Electron-hole plasma in 2D semiconductors

The Coulomb interaction can be screened by charge carriers, regardless of the origin of them (intrinsic, doped or photo-excited). At sufficiently high carrier densities, the Coulomb interaction between electrons and holes are so screened that the exciton is not the most energetically favorable species. Instead, the high density electrons and holes behave like free carriers, termed electron-hole plasma. The transition between exciton and electron-hole plasma in photo-excited semiconductors is known as the exciton Mott transition, in analogy to the Mott insulator-metal transition in strongly correlated materials[9,25,26].

Both the single particle band gap and the exciton binding energy scales with the strength of Coulomb interaction. With increased screening, the single particle band gap will shrink, i.e. band gap renormalization. The exciton binding energy will usually shrink by a similar amount, keeping the exciton energy level nearly constant with increased carrier density. The Mott density can then be defined as the carrier density when the renormalized band gap is equal to the exciton energy level, i.e. the exciton binding energy equals zero[27]. At carrier densities higher than the Mott density, the exciton resonance still exist but is higher than the bottom of the electron-hole continuum. At the bottom of the renormalized band, the high density electrons and holes create population inversion yielding stimulated emission.

There is a general relation[28] between band gap renormalization scaled by exciton binding energy, $\Delta E_g/E_B$, and the inter-particle distance scaled by Bohr radius $r_s = \left(\pi n a_B^2\right)^{-1/2}$. The 2D systems are characterized by large exciton binding energy and band gap renormalization, but the scaled band gap renormalization is smaller than the 3D case for the same r_s[28], as expected from the reduced screening by the injected carriers confined in the 2D plane. It can be seen that when

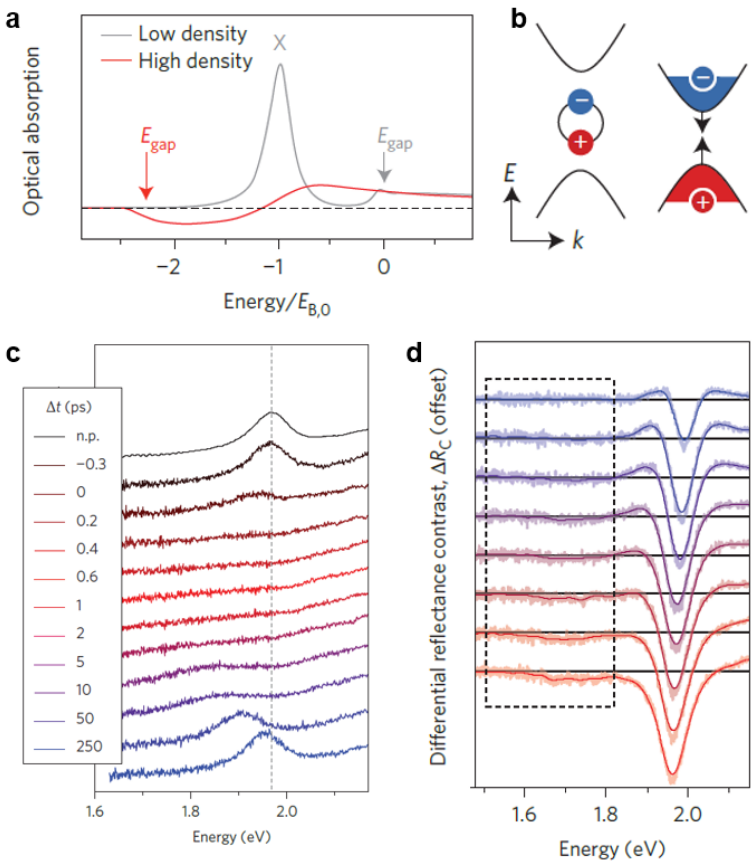

Figure 1.2 | Exciton Mott transition in TMDCs. a, The optical response across Mott transition. **b**, Illustration of exciton and electron hole plasma in reciprocal space. **c**, The disappearance and recovery of exciton absorption in time resolve reflectance contrast spectroscopy. **d**, The stimulated emission as a function of excitation density. Panels **a**, **b**, **c** and **d** adapted from ref. [29], Macmillan Publishers Ltd.

r_s = 1, i.e. when the inter-particle distance is equal to exciton Bohr radius, the band gap is already renormalized by more than $2E_B$. Therefore this criteria is an overestimation of the Mott density[9].

The Mott transition in 2D TMDCs was first demonstrated in monolayer and bilayer WS_2 in 2015 by time-resolved reflectance contrast spectroscopy[29]. For atomically thin materials on transparent substrate, the reflectance contrast is proportional to absorption[30]. In the high density reflectance contrast spectra, the exciton peak at low densities is replaced by broad and flat band to band absorption feature and negative absorption near the renormalized band gap. After a few picoseconds, the exciton feature starts to emerge and recover from lower energy[29]. The band gap

renormalization was estimated to be about 500 meV[29]. Further excitation energy dependent transient absorption studies illustrate the process of exciton Rydberg states merged by the renormalized band gap with increasing excitation density[31]. Time and angle resolved photoemission spectroscopy was used to directly measure the band gap after ultrafast high density excitation[32]. A decrease as much as 360 meV was directly measured in MoS_2 monolayers[32].

1.4 Interlayer excitons in 2D semiconductor heterostructures

The motivation of developing 2D materials, especially atomically thin 2D materials, is not only to study the physics at reduced dimensions; instead, the more important goal is to create unlimited amount of new materials with tunable properties from stacking different kinds of 2D components[33]. In addition to the stacking order, the recent success of superconductivity in magic angle twisted bilayer graphene has underscored the importance of twist angle, an unprecedented parameter in designing new materials[34,35].

In terms of 2D TMDCs, the band alignment of any combination between them is type-II (staggered). It implies that the photo-excited electrons and holes will prefer to reside in different layers in a heterostructure. Photoluminescence, transient reflectance, THz emission and time resolved photoemission studies have revealed the ultrafast time scale of this charge transfer[36–38]. In comparison to the picosecond (nanosecond) lifetime of charge recombination in monolayers (heterostructure), this charge separation is surprisingly efficient despite the van der Waals nature of interlayer coupling.

The separated charge carrier are Coulomb bound across the interface, leading to the formation of charge transfer excitons, or interlayer excitons to emphasize this atomic limit case. In the reciprocal space, the VBM and CBM at ±K valleys are offset by the twist angle between

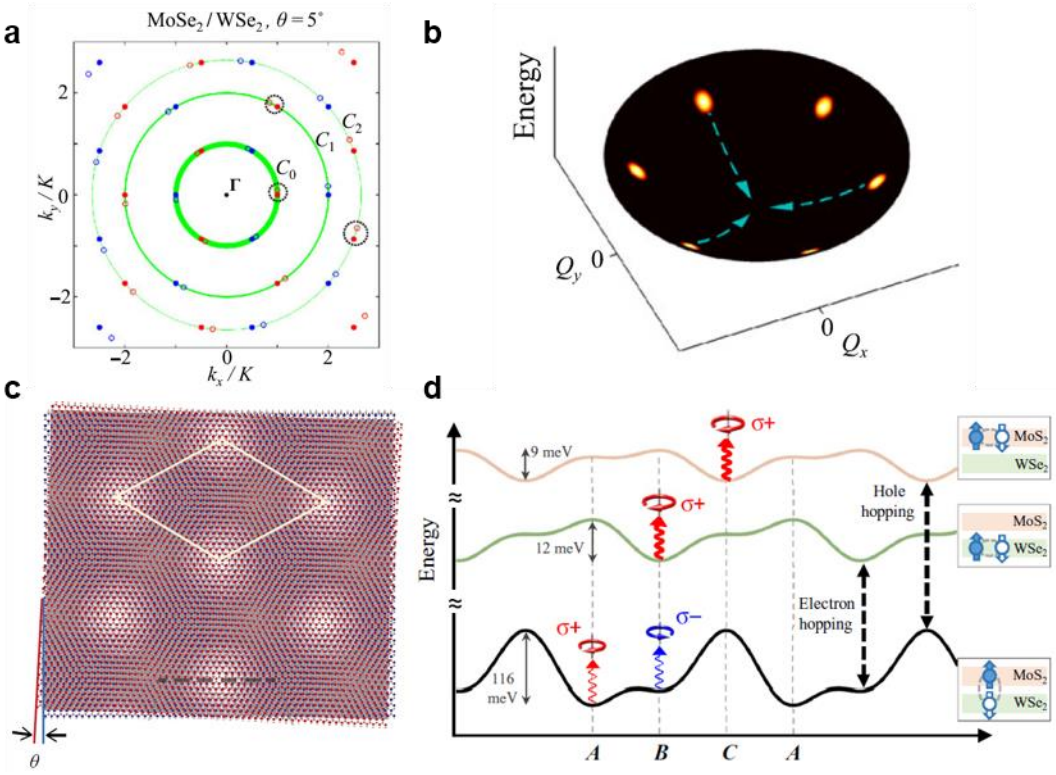

Figure 1.3 | Interlayer excitons in TMDC heterobilayers. a, The Brillouin zone of twisted heterobilayer. **b**, The interlayer exciton dispersion and light cones of twisted heterobilayers. **c**, Moiré superlattice of twist heterobilayers. **d**, Moiré potentials for intralayer and interlayer excitons. Panels adapted from: **a** and **b**, ref. [39], American Physical Society; **c**, ref. [40], Macmillan Publishers Ltd; **d**, ref. [41], under a Creative Commons License 4.0 (CC BY-NC).

two layers. The heterostructure band gap is indirect and the interlayer exciton is outside of the light cone unless the two layers are well-aligned[39]. The photoluminescence of the interlayer exciton is at a lower energy than intralayer excitons for such aligned TMDC heterostructures[42], consistent with the reduction of band gap by type-II band alignment. The absorption spectroscopy of interlayer excitons instead turns out to be extremely hard to measure due to the tiny overlap of quantum confined electron and hole wavefunctions. The only observation was made possible by photoconductivity and cross section of interlayer exciton is estimated to be more than two orders of magnitude smaller than that of the intralayer excitons[43]. In addition to

±K valleys, other valleys can also be involved in the formation of indirect interlayer excitons, the most confirmed of which consists the electron in Q valley and the hole in K valley[44,45].

Interlayer excitons can be used in optoelectronics and valleytronics. The electrical control of neutral or charged interlayer exciton flux are demonstrated[46,47]; interlayer exciton laser of extended spatial coherence is also achieved by placing aligned $MoSe_2/WSe_2$ heterobilayer on a silicon nitride grating resonator[48]. Valley polarized interlayer excitons in $MoSe_2/WSe_2$ heterobilayers are shown to have 40 ns lifetime[49]; more importantly, the valley polarized holes in WSe_2/MoS_2 heterobilayers improve the valley polarization to near-unity and extend the valley lifetime to more than 40 μs[50]. The TMDCs heterostructures are therefore a better platform than monolayers in valleytronics applications.

When the two layers are twisted by a finite angle, the difference in lattice momentum vectors forms a mini-Brillouin zone; in real space a moiré superlattice is formed with larger unit cell. The interlayer distance varies with the position in moiré supercell leading to a varying energy landscape with 100 meV well deepness[41]. At low densities, the interlayer excitons can be trapped in those moiré potentials forming a quantum dot array, as evinced by sharp features in photoluminescence[40]. The introduction of moiré picture enriches the interlayer exciton physics. It is predicted that the moiré exciton bands feature a topological structure with a Dirac node and two Weyl nodes connected by spin-momentum locked topological edge modes[41].

Finally, as an atomically thin limit of previously extensively studied coupled quantum wells[9], the TMDC heterostructures bear the expectation of realizing strongly correlated phenomena including exciton condensation, superfluidity and superconductivity. The heterostructure of two TMDCs separated by atomically thin BNs are predicted to rival the record critical temperature of cuprate superconductors because of its large binding energy and long

lifetime[51,52]. First signatures of such condensate have been observed in the sensitivity of electroluminescence to electron-hole imbalance in $MoSe_2$/BN/WSe_2 heterostructures[53].

1.5 Scope of this dissertation

This dissertation summarizes my work on the electron-hole system in 2D TMDC monolayers and their heterostructures. Chapter 2 reviews the experimental techniques developed and implemented in this dissertation. Chapter 3 discusses the twist angle dependence of interlayer charge transfer and recombination in MoS_2/WSe_2 heterostructures. Chapter 4 and 5 are devoted to the observation of Mott transition from interlayer exciton to charge separated electron hole plasmas in $MoSe_2$/WSe_2 heterostructures by spectroscopy (Chapter 4) and transport (Chapter 5) methods. Chapter 6 covers the study of the nature of trions in $MoSe_2$ monolayers. Chapter 7 concludes the dissertation with perspective of future work.

This page intentionally left blank

Chapter 2

Optical Spectroscopy

This chapter reviews the experimental techniques employed in this dissertation, with particular emphasis on (1) the design and implementation and (2) the applications to 2D semiconductors and their heterostructures. These techniques fall into the broad category of optical spectroscopy, with the general idea that the modification of light by light-matter interaction can be used to probe the properties of matter. 2.1 and 2.2 discuss the linear and nonlinear optical properties; 2.3 and 2.4 add temporal and spatial resolution to those spectroscopic techniques.

The optical spectroscopy is often advertised as versatile, non-invasive and easy to implement; however, it also bears some intrinsic limitations, such as the difficulty in assigning spectroscopic signatures, inability to detect transitions forbidden by selection rules and states outside the light cone, diffraction limited spatial resolution, transform limited pulse duration and photo-damage to samples. Therefore, a comprehensive understanding of light-matter interaction and a careful design of instrument and experiment are necessary to obtaining meaningful results from optical spectroscopy.

2.1 Absorption and photoluminescence

In classical electrodynamics theory, light is considered as an AC electric field **E** and the response of matter is described by the dipole moment per unit volume, or polarization **P**. In general, the polarization can be expressed as a power series in the electric field; linear optics then refers to the case when the polarization depends linearly on the electric field:

$$\mathbf{P} \propto \chi^{(1)}\mathbf{E}$$

The coefficient depends on the choice of unit system and convention[54]. In the following the absorption and photoluminescence spectroscopies are discussed.

In a direct bandgap semiconductor, the absorption spectrum is determined by transition matrix element $M \propto \langle \mathrm{f} | \mathbf{r} | \mathrm{i} \rangle$ and the joint density of states $g(\hbar\omega)$[55]:

$$\alpha(\hbar\omega) \sim |M|^2 \, g(\hbar\omega)$$

while the photoluminescence (PL) spectrum depends on one extra factor, the population of the excited state[55]:

$$I(\hbar\omega) \sim |M|^2 \, g(\hbar\omega) \times \text{level occupancy factors}$$

In 2D materials, the joint density of states is independent of energy[11].

The absorption spectroscopy of atomically thin materials are most conveniently measured by reflectance contrast. For a layer of material of thickness much smaller than the wavelength of light supported on a thick transparent substrate, the reflectance contrast is proportional to absorbance A:

$$\frac{\Delta R}{R} = \frac{R_{\text{sample}} - R_{\text{substrate}}}{R_{\text{substrate}}} = \frac{4}{n_{\text{substrate}}^2 - 1} A$$

where $n_{\text{substrate}}$ is the refractive index of the substrate[30]. If the sample is not much thinner than the light wavelength (e.g. BN encapsulated) or the substrate is not transparent (e.g. Si/SiO_2), the reflectance contrast spectrum is going to be distorted while still showing peaks at exciton resonances. The use of high NA objective, a common practice in 2D materials field, further shifts and broadens the features of the absorption spectroscopy.

The absorption (reflection, transmission) of a multilayer structure can be calculated by the transfer matrix method from the dielectric function. Here the modification of the forward and

backward propagating light waves by each layer is represented by a matrix; the total response is a special product of matrices of each layers. The interference effects are naturally taken into account in solving Maxwell equations. In reverse, the dielectric function can be retrieved from the absorption (reflection, transmission) by fitting with constrains imposed by Kramers-Kronig relations[56,57]:

$$\chi_1(\omega) = \frac{2}{\pi}\mathcal{P}\int_0^\infty \frac{\omega'\chi_2(\omega')}{\omega'^2-\omega^2}\mathrm{d}\omega$$

In this dissertation, the reflectance contrast and photoluminescence spectroscopies were mostly performed on a home-built reflection microscope system based on a liquid-helium recirculating optical cryostation (Fusion/X-Plane, Montana Instruments) with a 100×, NA 0.75 objective (Zeiss LD EC Epiplan-Neofluar 100×/0.75 HD DIC M27). The temperature of the sample stage could be varied between 3 and 350 K. The pressure of the chamber is in the high vacuum range. The spatially filtered and collimated white light from a 3200 K halogen lamp (KLS EKE/AL) was used for reflectance contrast measurements; the continuous wave (CW) laser at 532 nm (CNI) was used for PL measurements. Those lights can be focused to a diffraction limited spot on the sample by the objective, or focused to the back focal plane of the objective to create an even illumination on the sample. The reflected or emitted light was collected by the same objective, spectrally filtered, dispersed by a grating and detected by an InGaAs photodiode array (PyLoN-IR, Princeton Instruments). The excitation power was measured by a calibrated power meter (OPHIR StarLite) with broad dynamic range. The wavelength was calibrated by neon-argon and mercury atomic emission sources (IntelliCal, Princeton Instruments). The intensity was calibrated by three independent NIST traceable light sources: a 400 to 1050 nm tungsten halogen lamp (StellarNet SL1-CAL), a 250 to 2400 nm

quartz tungsten halogen lamp (Oriel 63355), and a 425 to 1000 nm LED (light-emitting diode) (IntelliCal, Princeton Instruments).

2.2 Second harmonic generation

Second order nonlinear optics refers to the case when the polarization scales quadratically with the electric field. The mixing of light frequency gives rise to several components. Second harmonic generation (SHG) is the generation of polarization at doubled frequency from mixing of two identical optical field where

$$\mathbf{P}_i^{(2)} \propto \sum_{j,k} \chi_{ijk}^{(2)} \mathbf{E}_j \mathbf{E}_k$$

The second order susceptibility $\chi^{(2)}$ is a third-rank tensor consisting of 27 components.

In contrast to bulk TMDCs, the monolayer TMDCs breaks inversion symmetry allowing a non-zero $\chi^{(2)}$; they indeed generate strong second harmonic, with effective volume $\chi^{(2)} \sim 10^{-21}$ C/V^2 (or 10^2 pm/V) comparable to that of absorbing nonlinear crystals[58]. SHG has thus been used to characterize the crystal orientation[58], which turns out vital in controlling the properties of heterostructure, thanks to the discovery of twistronics[34,35,40].

The symmetry of SHG of monolayer TMDCs originates from the symmetry of their $\chi^{(2)}$. As a third-rank tensor, for coordinate transformation

$$x^i = \frac{\partial x^i}{\partial \bar{x}^{i'}} \bar{x}^{i'}$$

$\chi^{(2)}$ transforms as

$$\bar{\chi}_{i'j'k'} = \frac{\partial x^i}{\partial \bar{x}^{i'}} \frac{\partial x^j}{\partial \bar{x}^{j'}} \frac{\partial x^k}{\partial \bar{x}^{k'}} \chi_{ijk}$$

If the coordinate transformation is a symmetry transformation, i.e. it recovers the matter of interest, $\chi^{(2)}$ should also be preserved:

$$\bar{\chi}_{i'j'k'} = \chi_{ijk}$$

Monolayer TMDCs belong to the D_{3h} point group. In the following the zigzag, armchair and out-of-plane directions are set as *x*, *y* and *z* directions. First consider the reflection about the *xy* plane, σ_h and the reflection about the *yz* plane, σ_v:

$$\bar{\mathbf{x}} = \begin{pmatrix} 1 & 0 & 0 \\ 0 & 1 & 0 \\ 0 & 0 & -1 \end{pmatrix} \mathbf{x} \text{ and } \bar{\mathbf{x}} = \begin{pmatrix} -1 & 0 & 0 \\ 0 & 1 & 0 \\ 0 & 0 & 1 \end{pmatrix} \mathbf{x}$$

All components of $\chi^{(2)}$ with odd numbers of *z* subscript or *x* subscript are eliminated. Consider the reflection about another σ_v which is $\alpha = +\pi/6$ away from the *xz* plane:

$$\bar{\mathbf{x}} = \begin{pmatrix} \cos 2\alpha & \sin 2\alpha & 0 \\ \sin 2\alpha & -\cos 2\alpha & 0 \\ 0 & 0 & 1 \end{pmatrix} \mathbf{x}$$

One gets $\chi_{yzz} = \chi_{zyz} = \chi_{zzy} = 0$ as well as

$$\chi_{yyy} = -\chi_{yxx} = -\chi_{xxy} = -\chi_{xyx} \equiv \chi$$

which are the only non-zero components of $\chi^{(2)}$ for materials in D_{3h} point group[54].

From the symmetry of $\chi^{(2)}$, the components of polarization **P** in monolayer TMDCs under fundamental optical field **E** at normal incidence can be derived:

$$\begin{aligned} P_x &= \chi_{xxy} E_x E_y + \chi_{xyx} E_y E_x = -2\chi E^2 \sin\theta\cos\theta = -\chi E^2 \sin 2\theta \\ P_y &= \chi_{yxx} E_x E_x + \chi_{yyy} E_y E_y = \chi E^2 \left(\sin^2\theta - \cos^2\theta\right) = -\chi E^2 \cos 2\theta \\ P_z &= 0 \end{aligned}$$

where θ is the angle between **E** and *x* direction. The polarization vector **P** is in the *xy* plane, with amplitude χE^2 and azimuthal angle $\left(-2\theta - \frac{\pi}{2}\right)$. The components of **P** parallel and perpendicular to **E** are

$$P_{\parallel} = P_x \cos\theta + P_y \sin\theta = -\chi E^2 \sin 3\theta$$
$$P_{\perp} = -P_x \sin\theta + P_y \cos\theta = -\chi E^2 \cos 3\theta$$

The angle between **P** and **E** is $\left(-3\theta - \frac{\pi}{2}\right)$.

The symmetry of SHG intensity signal depends on experimental geometry. If the sample is rotating while the laser and detection polarizations are fixed (geometry I), or if the sample is fixed while the laser and detection polarizations are rotating in phase (geometry II), the angle of rotation are relative between fundamental and SHG polarizations and the norm of parallel and perpendicular components of **P** are effectively measured, with a six-fold symmetry[58]:

$$I_{\parallel} \propto P_{\parallel}^2 = \chi^2 I_0^2 \sin^2 3\theta$$
$$I_{\perp} \propto P_{\perp}^2 = \chi^2 I_0^2 \cos^2 3\theta$$

If the sample and detection polarization are fixed while the laser polarization is rotating (geometry III), the angle of rotation is referenced to the laboratory coordinates and the x and y components of P are effectively measured, with a four-fold symmetry[59]:

$$I_x \propto P_x^2 = \chi^2 I_0^2 \sin^2 2\theta$$
$$I_y \propto P_y^2 = \chi^2 I_0^2 \cos^2 2\theta$$

Geometry III is the most convenient setup with a rotating half waveplate for laser but convolves the most instrumental polarization response in the signal. To realize geometry I, an *xy* translational stage - rotational stage - *xy* translational stage - sample setup is required, since the center of objective, rotational stage and sample needs to be aligned. The major difficulty lies in the stability of rotational axis, which is required to be within the size of the sample. Nevertheless, geometry I is an ideal setup for macroscopic monolayers. For microscopic TMDC monolayers, geometry II turns out to be the best way for SHG characterization. Figure shows the setup of geometry II. A rotating achromatic half waveplate is placed between the objective and

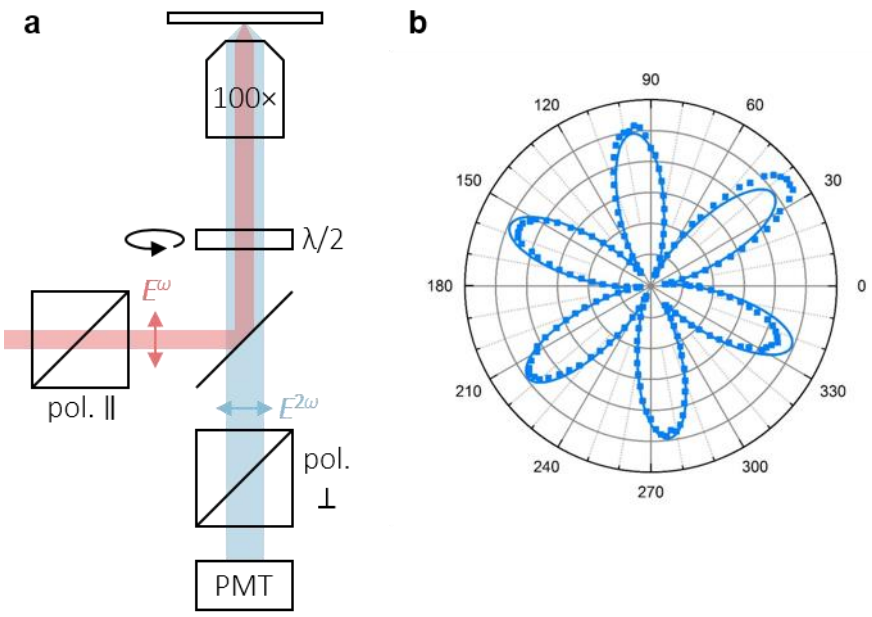

Figure 2.1 | Second harmonic generation. a, The SHG setup of geometry II. **b**, The six-fold pattern of TMDC SHG measured by the setup in **a**.

the short-pass dichromic mirror. Both the laser and the detection polarization are rotated in phase by this waveplate; the direction of the detection polarizer can be fixed at any angle relative to the laser polarization. After all, the offset angle from fitting SHG-angle curves and the photo taken by the same objective is correlated by measuring chemical vapor deposition grown triangular TMDC flakes where the edges correspond to zigzag directions.

It is worth noticing that TMDC monolayers have three-fold symmetry. The opposite directions become indistinguishable in above-mentioned experiments since by measuring the SHG intensity only the amplitude of the polarization is measured. Interferometry with a second reference SHG pulse at fixed polarization will preserve the sign of polarization in the signal[60].

Other than characterizing crystal orientation, SHG can also be used in energy-resolved way to identify the Rydberg exciton resonances in TMDC monolayers[61]; in addition, SHG can be

used as a probe of symmetry change[59] and electric field[62] in TMDC monolayers and heterostructures.

2.3 Time-resolved spectroscopy

To obtain time-resolved dynamics, the system of interest needs to be first driven out of equilibrium by a pump pulse. Then there are two approaches to add time resolution, depending on the nature of the probe signal. If the probe signal is from spontaneous emission with a finite lifetime, a gate pulse is used to control time window of detection. This approach is usually used in measuring time-resolved photoluminescence, such as time-correlated single photon counting (TCSPC) or streak camera (where the gate pulse is electronic) and Kerr-gating or up-conversion (where the gate pulse is optical). If the probe signal is an instantaneous response of an optical pulse, the response can be directly detected in a continuous or modulation way while the pump-probe pulse delay provides the time axis. This approach is usually used in transient absorption/reflectance or time-resolved SHG. The TCSPC and transient reflectance used in this dissertation are discussed below.

The technical details of TCSPC can be found in the bh TCSPC handbook[63]. Here I provide a brief overview of its principles. In such experiments, an avalanche photodiode (APD) is often used to detect single PL photons. The electronic pulses from ultrafast laser and single photon detector are both sent to the TCSPC card. The constant fraction discriminators (CFD) are used to determine the appearance of those pulses. The use of CFD avoids pulse-height induced timing jitter. The output pulse of CFD from the single photon pulse will trigger the charging of a capacitor, the time-to-amplitude converter (TAC); the reference pulse from laser will stop the charging. This reverse start-stop configuration prevents resetting the TAC for every repetition cycle. The voltage of TAC reflects the difference of arrival times between single photon pulse

and laser pulse. This amplified TAC output is converted to delay time by the analog-to-digital converter (ADC) and the corresponding time channel in memory accumulates one more event. This process is repeated for many repetition cycles when the delay times of single PL photons are recorded. The photon count as a function of delay time represents the probability of emission after pulsed excitation, i.e. time-resolved PL.

Since only the first photon can be detected for every cycle, the PL intensity at the APD is kept so low that keep the probability of detecting two photons per cycle is within acceptable error. The instrument response function (IRF) of TCSPC can be determined by recording the reflected ultrafast laser pulse (< 100 fs). The IRF has a full width at half maximum (FWHM) of 120 ps, corresponding to a time resolution of about 20 ps.

In transient reflectance experiments, the relative change of probe pulse reflectance after pump pulse excitation was measured as a function of pump-probe delay:

$$\frac{\Delta R}{R}(t) = \frac{R(t) - R_0}{R_0} = \frac{I(t) - I_0}{I_0}$$

where R_0 is probe pulse reflectance, $R(t)$ is probe pulse reflectance after time $\boldsymbol{t}$ of pump pulse excitation, I_0 and $I(t)$ are the reflected probe pulse intensity without and with pump pulse excitation. For < 1ns delay time, the pump-probe delay is controlled by a delay stage through varying the length of light path of pump or probe beam. Since the relative change is usually small, the modulation technique is used to reduce the noise, where the difference signal is brought to a finite frequency. To this end, a chopper is used to turn on / turn off pump pulse and the detection is synchronized with the chopper. There are two types of detection mechanism depending on the number of probe channels.

If a single channel of probe is detected, a lock-in amplifier (LIA) can be used to detect the small difference. Interested readers are referred to the manual of SR830 LIA[64]. The probe

signal is a periodic square wave at chopping frequency ω with a large offset. Consider the sinusoidal component at ω of the probe signal:

$$V(t) = V\sin(\omega t + \theta) + V_0$$

with a amplitude V and offset V_0. In the LIA, the probe signal is filtered and amplified before mixing with the reference signal at ω from chopper using a phase sensitive detector (PSD):

$$\begin{aligned} V_{\text{PSD}}(t) &= V(t)V_{\text{ref}}(t) \\ &= \left(V\sin(\omega t + \theta) + V_0\right)\cdot V_{\text{ref}}\sin(\omega t + \theta_{\text{ref}}) \\ &= \frac{1}{2}VV_{\text{ref}}\cos(\theta - \theta_{\text{ref}}) - \frac{1}{2}VV_{\text{ref}}\cos(2\omega t + \theta + \theta_{\text{ref}}) + V_0V_{\text{ref}}\sin(\omega t + \theta_{\text{ref}}) \end{aligned}$$

The mixing of two signals at ω generates a DC component and a 2ω component; The DC offset of probe signal is shifted to frequency ω. Low-pass RC filters then filter out all the AC components, leaving the DC component that is proportional to the amplitude V:

$$\left|\frac{V_{\text{out}}}{V_{\text{in}}}\right|^2 = \left(\frac{1}{1+(2\pi f\tau)^2}\right)^n$$

The time constant τ and number of filters n (related to the slope) can be tuned for the best filtering performance. The phase difference term is eliminated by first measuring the modulated pump signal and maximizing the output by varying θ_{ref}. Once determined the θ_{ref} is locked by the phase-locked-loop and used in pump-probe experiments. An 1 V pump-induced difference corresponds to a sinusoidal component amplitude $V = 2/\pi$ V and a LIA output of $\sqrt{2}/\pi$ Vrms. This output is reached exponentially with a time constant τ set by the RC filters. The absolute voltage of probe signal can be measured by the auxiliary channel of LIA in order to obtain the percentage of relative change.

If the probe signal has multiple channels, the detector must be synchronized with the chopper to make measurements at 2ω frequency, i.e. one on and off spectrum for each

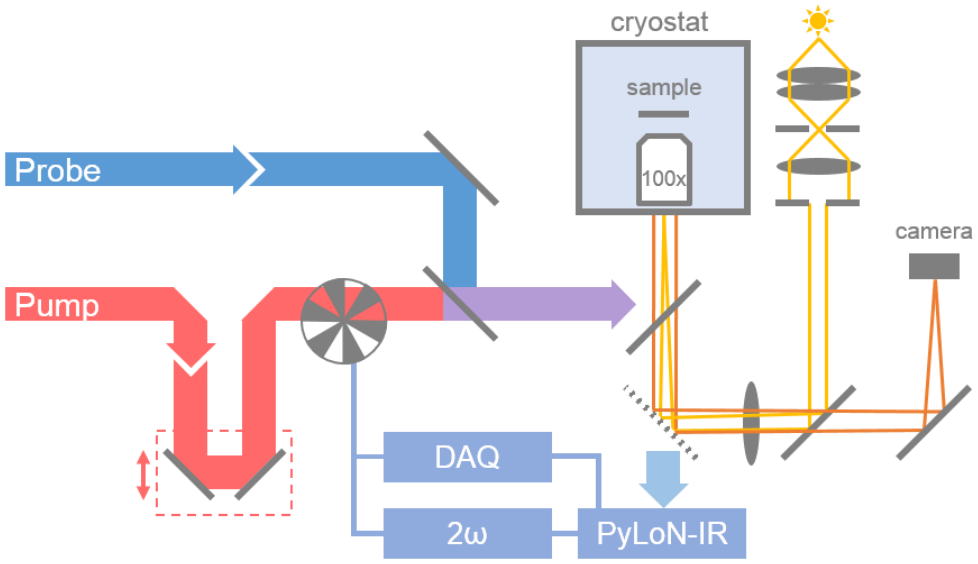

Figure 2.2 | The pump-probe setup coupled with wide-field helium-temperature microscope.

modulation cycle. In this dissertation, an InGaAs photodiode arrary (PyLoN-IR, Princeton Instruments) was used for spectrally resolved transient reflectance at near-IR region. A homemade frequency double is used to obtain doubled frequency from chopper reference. The square wave output from chopper is first delayed by RC filtering and thresholding; the original and delayed waves are sent to an XOR gate to generated square pulses at doubled frequency. This doubled frequency is used to trigger the camera. The sign of the transient reflectance signal is determined by recording the chopper reference wave with a data acquisition card (National Instruments) triggered by the camera.

This setup was optimized to detect down to 10^{-4} change in the near-IR region. The chopper modulation frequency was selected to maximize the signal-to-noise ratio of transient reflectance signal. While the high modulation frequency is often preferred to remove the $1/f$ noise, in the case of weak probe and digital detection, it is important that the modulation frequency is low enough to ensure enough probe signal being recorded at each cycle. The chopper reference wave is detected at a different position from where the pump passes. This

phase difference needs to be determined by scanning the added phase of the chopper electronically. While the synchronization with laser pulses is recommended, in the case when this synchronization is not available, the effect of including one more or less pulse in half a modulation period should be within error. Finally, the supercontinuum white light probe, here generated by focusing the femtosecond laser pulses from the Ti:sapphire regenerative amplifier (Coherent RegA 9050, 250 kHz, 800 nm, 100 fs) onto a 3-mm sapphire crystal, needs to be finely tuned and filtered to obtain a stable and flat white light spectrum, especially near the fundamental wavelength. The cross-correlation of pump and probe pulses, measured by sum frequency generation on a gold surface, has a FWHM of 220 fs, corresponding to a time resolution of about 40 fs.

2.4 Imaging

The size of TMDC monolayers are usually in the range of several to tens of micrometers which requires microscopy to be seen and optically measured; spatial inhomogeneity in 2D monolayers and heterostructures necessitate mapping of samples as a basic characterization; study of transport by optical spectroscopy needs spatial control and monitoring of electronic species. Therefore, adding spatial resolution to optical spectroscopy is necessary for studying 2D semiconductors and their heterostructures. In fact, their atomically flat surface is well-suited for 2D imaging experiments. This section serves as a brief overview of the wide-field microscopy and scanning confocal microscopy the author designed and implemented for the works in this dissertation. Interested readers are referred to Handbook of Biological Confocal Microscopy for detailed technical considerations.

The key idea behind modern imaging systems is that a single lens does Fourier transform between its two focal planes. This can be seen from simple ray tracing of a single lens: parallel

light rays from different points in one focal plane focus onto one point at different directions in the other focal plane, and vice versa. Therefore, the positions in one focal plane translate into momenta in the other focal plane. This simple observation immediately lead to two important results. First, a scanning mirror at Fourier plane can direct the light ray to different positions in the sample plane, simply by taking different angles of reflection. The image can be reconstructed by associating signals at different angles to corresponding coordinates. Second, a second lens that does Fourier transform again will retrieve the image. In modern imaging systems, the lenses are placed in sequence with a common focal plane between two adjacent lenses, forming a telecentric system. This creates alternating planes of images and Fourier transformed images. The telecentric system is preferred because it is space invariant, linear and determined by a single parameter of magnification factor.

In the wide-field microscope, the sample is evenly illuminated and imaged in reflection geometry (epi-illumination). The even illumination is achieved by Fourier transforming the light source and placing the Fourier image on the sample (Köhler illumination). The white light from a fiber is first collected and imaged as a start of the telecentric system. Its Fourier transform is relayed to the sample plane by the tube lens - objective system. The intensity and field size of the illumination are independently controlled by two irises placed at the image plane (aperture diaphragm) and Fourier plane (field diaphragm) of the light source. The reflected light from sample is imaged by the objective - tube lens system to a camera.

In the scanning confocal microscope, the image of probe signal is first Fourier transformed to the back focal plane by the objective. This Fourier plane is then imaged by the tube lens - scan lens system so that an accessible pivot point is on the center of a dual-axis galvo mirror scanning system. The spatial scanning of the sample was achieved by scanning the angles

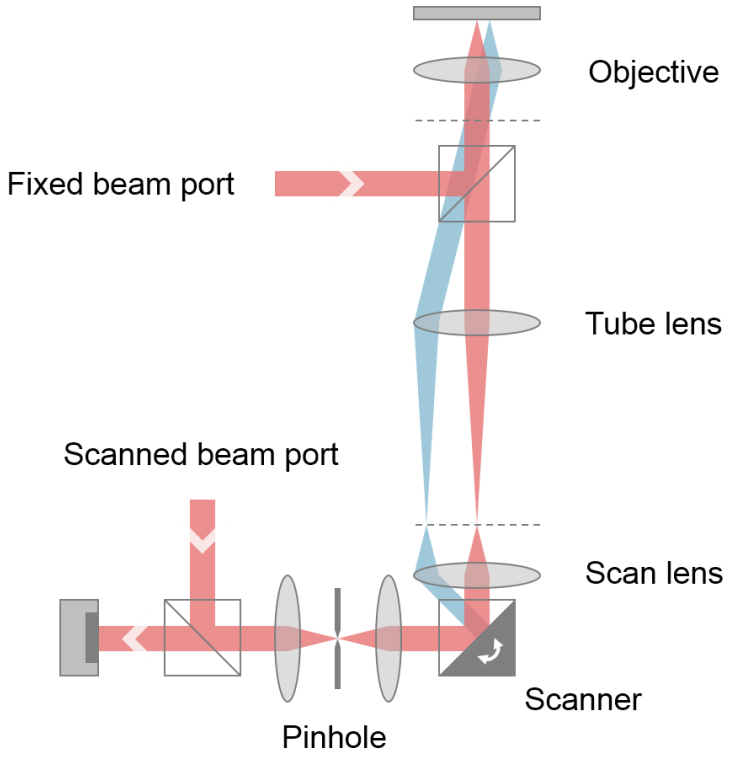

Figure 2.3 | The scanning confocal microscope with fixed and scanned beam ports.

of the galvo mirrors. The sample was imaged to a second image plane where a pinhole selects only the spot of interest (confocal). The pump light path depends on the type of experiment: in the mapping-type experiments, the pump/excitation and probe/detection spot was scanned together with a shared light path between the sample and the dichroic mirror; in the diffusion-type experiments, the pump/excitation spot was fixed while the probe/detection signal is still imaged by scanning.

The smallest spot of an optical system is limited by the diffraction of light. The diameter of the first dark ring of the diffraction image of a point source, Airy disk, is

$$d_{\text{Airy}} = \frac{1.22\lambda}{\text{NA}_{\text{obj}}}$$

where λ is the wavelength of light, $\mathrm{NA}_{\mathrm{obj}} = n\sin\theta$ is the numerical aperture of the objective. For an NA 0.75 objective, this diameter is 0.87 μm and 1.5 μm for 532 nm and 930 nm lights. The spatial resolution is $d_{\mathrm{Airy}}/2$ due to Rayleigh criterion.

The magnification factor of a telecentric system consisting of two lenses is

$$M = \frac{f_2}{f_1}$$

where f_1 and f_2 are focal lengths of the two lenses. The focal length of an objective is determined by its magnification factor and the focal length of its corresponding tube lens. For example, for Zeiss, the focal length of tube lens is 165 mm, so the focal length of an 100× objective is 1.65 mm. There are four important magnification effects in a scanning confocal microscope. The first is the magnification of the sample image on the pinhole plane (second image plane). The size of the pinhole should match the desired size of spot on the sample plane. In our system, the 1.65 mm objective is paired with a 200 mm tube lens, 50 mm scan lens and 50 mm achromatic lens to image the sample onto a pinhole, thus the magnification factor on the pinhole plane is 121. A 200 μm pinhole corresponds to an 1.65 μm spot size, roughly matching the size of the Airy disk. The second is the magnification of the sample image on the first image plane. The size of the desired image, together with the focal length of the scan lens, determines the correlation between scan angle and distance on sample plane:

$$\Delta x = \frac{f_{\mathrm{scan}} f_{\mathrm{obj}} \tan(2\alpha)}{f_{\mathrm{tube}}} \approx \frac{2 f_{\mathrm{scan}} f_{\mathrm{obj}}}{f_{\mathrm{tube}}} \alpha$$

A spot 1 μm away from the center of the sample corresponds to a scan angle of 0.0012 rad (0.069°). The third is the magnification of the distance between scanning mirrors and the pivot point. These two scanning mirrors for *x* and *y* directions cannot be both placed at the pivot point

and the laser beam will be moving slightly on the back focal plane during scanning. The magnification in the out-of-plane direction is

$$\Delta z' = M^2 \Delta z$$

For a scanning mirror placed 7.35 mm away from the pivot point, the image of the scanning mirror by the 4× system of scan lens - tube lens is 117.6 mm away from the back focal plane. To scan 20 μm away from the center of the sample plane, the angle of the beam at the back focal plane is about 0.012 rad, and the beam is going to drift 1.4 mm away from the center of the back pupil. The fourth is the magnification factor of the pump laser beam. The even part of the laser beam should always fulfill the back pupil to ensure a constant transmitted power. In our system, the laser beam was magnified 4 times to about 12 mm by the scan lens - tube lens system. The back pupil of 4 mm is therefore always fulfilled even considering the drift caused by using two scanning mirrors.

Chapter 3

Carrier Dynamics in MoS_2/WSe_2 Heterobilayers*

Interfacial charge separation and recombination at heterojunctions of monolayer TMDCs are of interest to two-dimensional optoelectronic technologies. These processes can involve large changes in parallel momentum vector due to the confinement of electrons and holes to the K valleys in each layer. Because these high-momentum valleys are usually not aligned across the interface of two TMDC monolayers, how parallel momentum is conserved in the charge separation or recombination process becomes a key question.

In this chapter we probe this question using the model system of a type-II heterojunction formed by MoS_2 and WSe_2 monolayers and the experimental technique of femtosecond pump-probe spectroscopy. Upon photoexcitation specifically of WSe_2 at the heterojunction, we observe ultrafast (<40 fs) electron transfer from WSe_2 to MoS_2, independent of the angular alignment and thus momentum mismatch between the two TMDCs. The resulting interlayer charge transfer exciton decays via non-radiative recombination with rates varying by up to three-orders of magnitude from sample to sample but with no correlation with interlayer angular alignment. We suggest that the initial interfacial charge separation and the subsequent interfacial charge recombination processes circumvent momentum mismatch via excess electronic energy and via defect-mediated recombination, respectively.

* This chapter is based on work published[87]: *Nano Lett.* **17**, 3591-3598 (2017). Copyright 2017, American Chemical Society.

3.1 Sample preparation and characterization

In a type-II heterojunction, exciton created by photoexcitation in one layer can dissociate by rapid electron or hole transfer across the interface (Figure 3.1a). Because of reduced dielectric screening in 2D, a spatially separated electron hole pair across the interface forms interlayer charge transfer (CT) exciton with binding energy >100 meV.[65,66] Previous studies have shown ultrafast (≤100 fs) interfacial CT processes in several 2D heterojunctions with arbitrarily aligned crystallographic orientations,[36] but radiative recombination likely only occurs for small angular mismatches (<5°) as defined by the so-called light cones.[39]

Because the conduction band minimum (CBM) and valence band maximum (VBM) in TMDCs are located at K points in momentum space with large parallel momentum vectors, the interfacial charge transfer process can be accompanied by large momentum change, Figure 3.1b. Similar to inter-band scattering or electron-hole recombination in indirect band gap bulk semiconductors,[9] the rates of charge separation and recombination across a TMDC hetero-interface should strongly depend on the magnitude of momentum change and phonon population (temperature). Because the angular alignment at 2D van der Waals heterojunctions is quantitatively controllable,[58] a central question is whether or how the crystallographic alignment, thus the momentum mismatch, affect interfacial charge separation and recombination in 2D heterojunctions.

Here we experimentally examine the influence of interlayer twist angle ($\Delta\phi$) on the interfacial charge transfer dynamics at MoS_2/WSe_2 heterojunctions. MoS_2/WSe_2 forms a type II heterojunction with conduction band offset of 0.76 eV (CBM of the composite interface in MoS2) and valence band offset of 0.83 eV (VBM in WSe2).[67] We prepared WSe2/MoS2 heterojunctions with $\Delta\phi$ varying in the complete range of 0-30° using mechanical exfoliation and

van der Waals stacking.[68] We probe photo-induced electron transfer from WSe_2 to MoS_2 and subsequent interlayer charge recombination using optical pump-probe spectroscopy. We observe ultrafast (<40 fs) interfacial electron transfer from WSe_2 monolayer to MoS_2 monolayer, independent of twist angle $\Delta\phi$. The interlayer charge recombination occurs on a much longer time scale and varies significantly from sample to sample (from ~40 ps to ~3 ns) but showing no clear correlation with twist angle $\Delta\phi$. Exciton/carrier density-dependent studies rule out the Auger scattering for interlayer excitons with excitons or doped carriers. These results can be well explained by the initial ultrafast resonant charge transfer across the interface with excess energy after photoexcitation and subsequent defect assisted non-radiative electron-hole recombination across the interface.

We prepared WSe_2/MoS_2 heterojunctions by mechanical exfoliation and the polydimethylsiloxane (PDMS) transfer technique[69] (for the gated sample only) or the hexagonal boron nitride (h-BN) pickup/transfer technique[70] for all other samples. The BN-pickup approach here can minimize the contamination and traps introduced during heterostructure preparation and minimize the effect of ambient (e.g., H_2O, O_2) on sample properties.[12] Figure 1c shows optical image of a WSe_2/MoS_2 heterojunction on the SiO_2/Si substrate. This architecture allows us to access and characterize both the monolayer regions and heterojunction region. To determine the twist angle $\Delta\phi$ between WSe_2 and MoS_2, we measured the intensity of linear-polarized second harmonic generation (SHG) as a function of crystal rotational angle ϕ, Figure 1d. We fit the angular-dependent SHG intensity with 6-fold symmetry. For all the heterostructure samples used, the interlayer twist angle $\Delta\phi$ varies between 0 and 30°. Unlike the valence band edges with large spin-orbital (SO) splitting (~150 and ~450 meV for molybdenum[71] and tungsten dichalcogenides,[72] respectively) and spin-valley coupling, the conduction band edges with

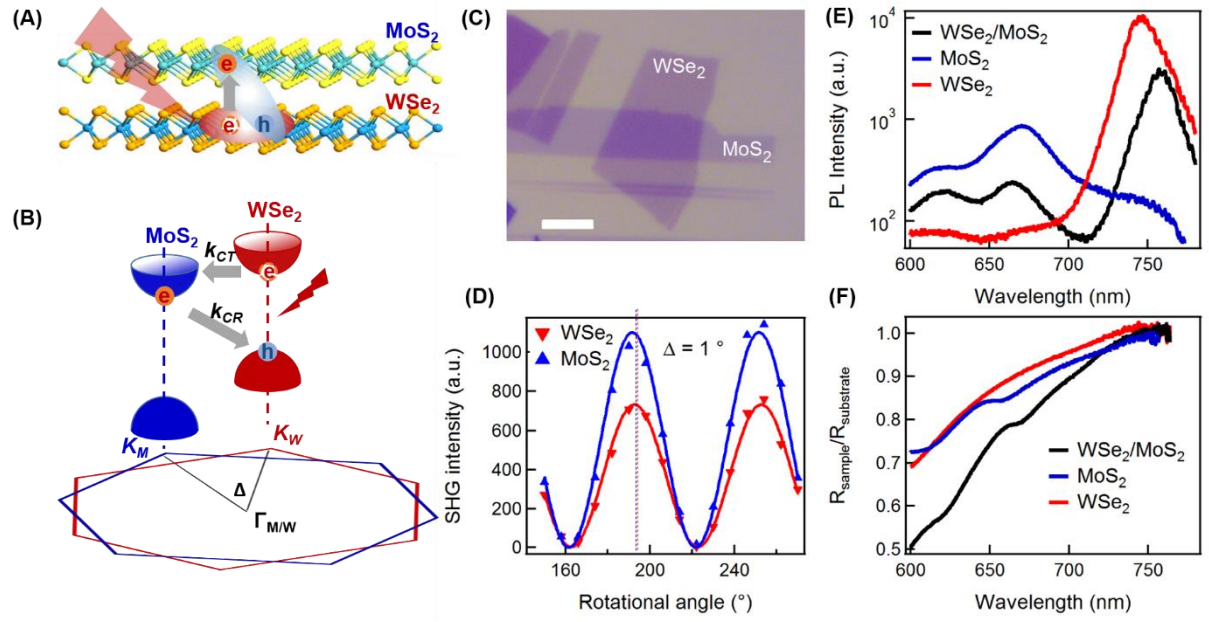

Figure 3.1 | Preparation and characterization of MoS_2/WSe_2 heterobilayers. a and **b**, Schematic illustration of MoS_2/ WSe_2 heterojunction where photoexcitation creates intralayer exciton in WSe_2 followed by electron transfer to MoS_2, forming indirect CT exciton in real space (**a**) and in momentum space (**b**). $\Delta\phi$ (between 0 and 30°) is the twist angle of relative crystallographic orientations or momentum space orientations for two monolayers. **c**, Optical image of stacked WSe_2/MoS_2 heterojunction. Scale bar: 5 μm. **d**, SHG intensity from WSe_2 and MoS_2 monolayer regions as a function of crystal's rotational angle after stacking. The rotational angle starts from arbitrary value. The fits allow us to determine $\Delta\phi$ values to ±1°. e and f, Photoluminescence (**e**) and reflectance (**f**) measurements of the WSe_2 monolayer, the MoS_2 monolayer, and the MoS_2/WSe_2 heterojunction regions, respectively.

opposite spins in MoS_2 or WSe_2 monolayer are nearly degenerate (SO splitting of 4 meV for MoS2 conduction band edges[71]). Therefore, we can assume 6-fold symmetry for electron in K and K′ valley conduction band edges and $\Delta\phi$ = 0° (30°) corresponds to the smallest (largest) momentum change for electron transfer from the WSe_2 K valley to the MoS_2 K valley. The same is true for subsequent recombination of an electron in MoS_2 with the hole left in WSe_2 at longer time scales. On the basis of the lattice parameters of MoS_2 (3.2 Å) and WSe_2 (3.3 Å), we obtain

the momentum change from the K valley in one layer to the K valley in another as $\Delta K_{\parallel} = 0.07$ and 1.25 $Å^{-1}$ for $\Delta\phi = 0°$ and 30°, respectively.

We characterized the as-prepared WSe_2/MoS_2 heterojunctions with PL and reflection spectroscopy. The PL and reflection spectra ($R = R_{sample}/R_{substrate}$) of monolayer regions and heterojunction regions are shown in Figure 1e,f, respectively. The reflection spectrum of MoS_2 monolayer shows two clear dips at ~658 and ~610 nm, corresponding to the A and B excitonic resonances, respectively.[1] The WSe_2 monolayer does not show any distinct reflection peak (or dip) but a broad feature at ~745 nm, corresponding to the WSe_2 A exciton transition.36 The opposite contribution of MoS_2 and WSe_2 excitonic resonance in the reflection spectrum results from an interference effect from the substrate SiO_2 layer; this will also affect the sign of transient reflection signal discussed later. These excitonic features in the reflection spectrum are slightly red-shifted and broadened in the heterojunction region. The PL spectra of the monolayer regions show emission peaks from the A and the B excitons in MoS_2 and the A exciton in WSe_2. These emissions are significantly quenched in the heterojunction region (note the logarithmic intensity scale), suggesting efficient interfacial CT processes. A careful examination of PL spectrum in the near-IR range (800-1700 nm) shows no interlayer CT exciton emission, suggesting the dominance of non-radiative recombination of the interlayer electron-hole pair in our samples. This issue will be discussed in detail later.

3.2 Carrier dynamics by transient reflectance

We probe interfacial charge separation and subsequently charge recombination processes at the WSe_2/MoS_2 heterojunction using pump-probe transient reflectance spectroscopy. We first excite the sample using a femtosecond pulse and after a certain delay time, measure the reflection change ($\Delta R/R$) of a broadband probe pulse. Herein, we use 710 nm light to only excite

the lowest energy A exciton in the WSe_2 monolayer to initiate the electron transfer from WSe_2 to MoS_2.We first investigate the exciton dynamics in WSe_2 monolayer region by probing the WSe_2 A exciton transition (W probe).The transient reflection spectrum of WSe_2 monolayer after photoexcitation shows a negative transient reflection peak at ~741 nm, corresponding to the bleach of A exciton resonance in WSe_2 monolayer due to the band filling of photo-excited excitons. The transient reflection signal rises promptly within experimental time resolution and its decay can be fitted by a bi-exponential function consisting of a 1.5 ps component (40%) and a 16.8 ps component (60%) with an average exciton lifetime of ~16 ps (green square/line in Figure 3.2d). This lifetime is similar to the values reported previously[73,74] and is significantly shorter than the exciton radiative lifetime at room temperature (nanosecond).[75,76] The much shorter lifetime for the WSe_2 monolayer probed here can be ascribed to defect mediated non-radiative e-h recombination.[73]

Figure 3.2b shows a transient reflection spectrum in the MoS_2 transition range (M probe, red triangles) obtained at 0.5~0.8 ps after photoexcitation of WSe_2 in the heterojunction. The positive peak at ~675 nm corresponds to bleach of the MoS_2 A exciton transition (the excitonic resonance shows a dip in reflection spectrum, Figure 3.1f). In control experiments, we observe negligible signal in this wavelength range from the MoS_2 or WSe_2 monolayer region following photoexcitation at the same wavelength (710 nm). As comparison, we also show a difference reflectance spectrum, black curve in Figure 3.2b, from the n-type gate-doping of MoS2 in the heterojunction. Here the difference reflectance spectrum is obtained from subtracting $R_{sample}/R_{substrate}$ at gate bias V_g = +50 V by that at V_g = 0 V. The excellent agreement between the transient reflectance spectrum from photo-exciting WSe2 in the heterojunction and difference reflectance spectrum from n-type gate-doping unambiguously confirms electron transfer from

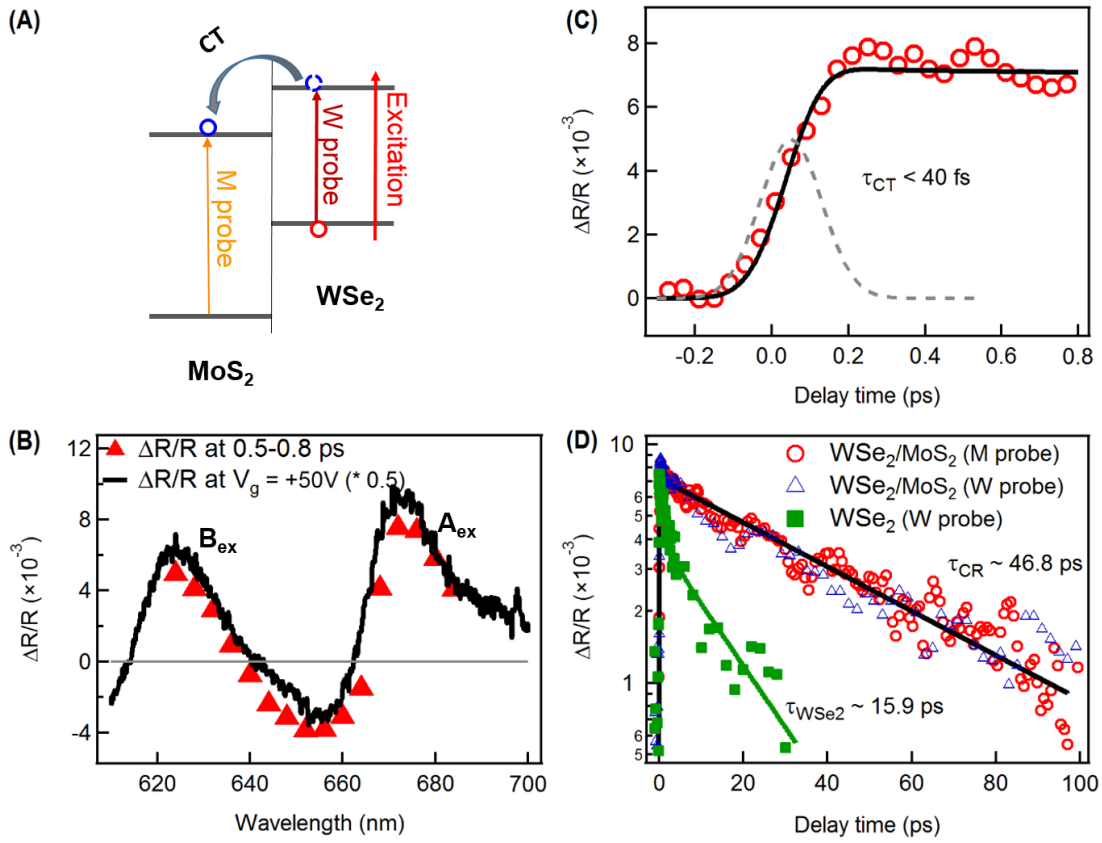

Figure 3.2 | Carrier dynamics by transient reflectance. a, Scheme illustration of pump-probe measurement. We exclusively excite the A exciton in WSe2 and probe MoS_2 (M probe) and WSe_2 (W probe) excitonic transitions, respectively. **b**, Transient reflection spectrum (red triangle) after electron transfer (delay time 0.5~0.8 ps) and its comparison with reflection spectrum change of the heterojunction gate-doping at V_g = +50 V (black curve), confirming photo-excited electron transfer from WSe_2 to MoS_2. (C) Early time (<1 ps) transient reflection kinetics from probing the MoS_2 transition with excitation of the WSe2 A exciton, showing ultrafast electron transfer rate (<40 fs). Gray dashed line is the pump−probe cross correlation function with FWHM ~190 fs. **d**, Comparison of heterojunction kinetics under M probe and W probe condition at later times (up to 100 ps), showing interlayer electron-hole recombination process at the heterojunction. Also shown is the transient reflection kinetics of WSe2 monolayer with a much shorter lifetime.

WSe_2 to MoS_2 while the hole stays in the former. Generally, the injected electrons in the MoS_2 layer can affect its excitonic transitions in multiple ways[9], including band filling (Pauli blocking), Coulombic screening, band renormalization, and the unique exciton-to-trion conversion in 2D monolayers.[14] Regardless of the detailed mechanism, electron transfer to MoS_2 is reflected by an overall bleach of the excitonic transitions in MoS2. In the weak excitation regime probed here, we verify the initial transient reflection signal amplitude (at ~0.5 ps) shows a linear dependence on excitation density ($\leq 5\times10^{11}$ cm^{-2}). Therefore, we take $\Delta R/R$ as proportional to electron population in the MoS_2 layer and probe the interfacial charge transfer dynamics.

Figure 3.2c shows the early time dynamics (red circles) probed at ~675 nm (bleach maximum of the MoS2 A exciton) following photoexcitation of WSe_2 in the heterojunction. Also shown is the pump-probe laser cross-correlation (CC, gray dashed curve) with FWHM ~190 fs, as well as time-convoluted CC (black curve) that represents prompt rise in signal within experimental time resolution. The excellent agreement between experimental data (red triangles) and convoluted CC (black curve) establishes that electron transfer from photo-excited WSe_2 to MoS_2 occurs on the ultrafast time scale ≤40 fs (experimental time resolution, ~1/5 of the FWHM), which is in agreement with previous estimates from pump-probe spectroscopies[36,77] and absorption peak broadening.[78]

In the interfacial electron transfer process, the hole stays in the WSe_2 layer, as confirmed by a bleach of the WSe_2 excitonic transition position. We use $\Delta R/R$ at the WSe_2 transition (W probe, ~ 754 nm) to follow hole population in the WSe_2 layer. Because of reduced dielectric screening in a 2D system, the hole left in WSe_2 and the electron transferred to MoS_2 should form an bound interlayer CT exciton with binding energy >100 meV.[65,66] We compare the electron

(red circles) and hole (blue triangles) decay dynamics in Figure 3.2d. The same dynamics with a single exponential fitted lifetime of τ_{CR} = 47 ± 9 ps, confirms that interlayer CT exciton decays through interfacial electron-hole charge recombination (CR). The CR process occurs with a ~ 3 times longer lifetime than that for the non-radiative exciton recombination in the WSe_2 monolayer, due to the spatially indirect nature of the CT exciton in the former.

3.3 Twist angle dependence of carrier dynamics

We probe the dependence of interfacial charge transfer on the angular alignment (and thus parallel momentum mismatch) between the WSe2 and the MoS2 monolayer in the heterojunction using 12 samples with twist angle $\Delta\phi$ in the range of 0−30°. All the heterojunction samples probed here are encapsulated with h-BN capping layers, as shown by representative optical images for three h-BN capped WSe_2/MoS_2 heterojunction samples ($\Delta\phi$ = 7°, 17° , and 29°) in Figure 3.3a-c. The corresponding kinetics probing electron population in MoS_2 following photoexcitation of WSe_2 are shown in Figure 3.3d-f. Each kinetic profile is described by a prompt rise (≤40 fs) corresponding to ultrafast electron transfer from WSe_2 to MoS_2, and a much slower decay from interlayer charge recombination which can be fitted by a single exponential function. The lifetimes of interfacial CT and CR processes for all samples are shown in red semitransparent area and with blue symbols, respectively, as a function $\Delta\phi$ (bottom) or momentum change (top). Regardless of $\Delta\phi$, interfacial electron transfer in WSe_2/MoS_2 van der Waals heterojunctions all occurs on an ultrafast time scale within experimental time resolution (<40 fs). This CT time is much shorter than the A exciton lifetime in the WSe2 monolayer (16−68 ps in our samples), suggesting near-unity electron transfer efficiency at the van der Waals heterojunction. The charge recombination lifetime varies by almost 3 orders of magnitude from sample to sample, from ~47 ps to ~3 ns, but does not show

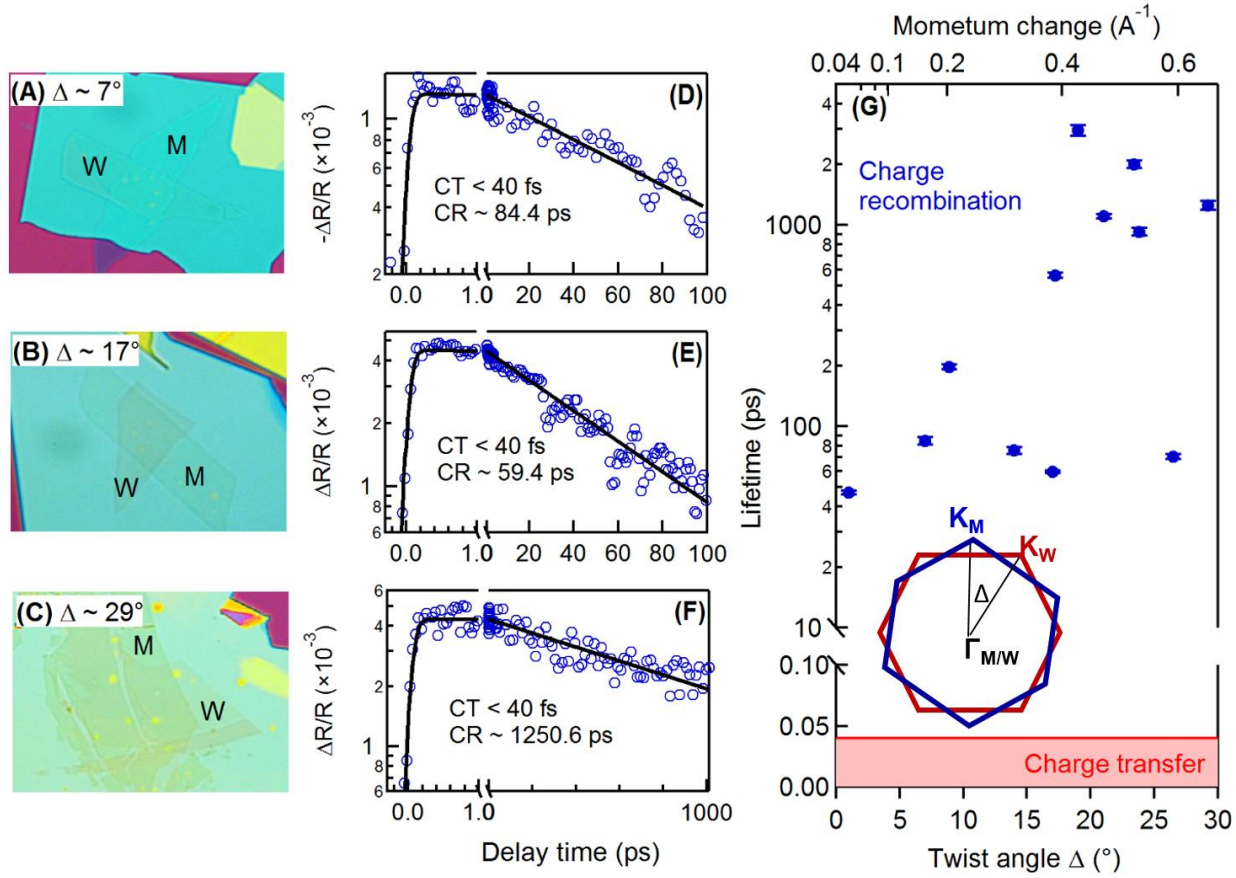

Figure 3.3 | Twist angle independent carrier dynamics. Optical images (**a-c**) and corresponding transient reflection kinetics in the MoS2 layer (**d-f**) for BN capped WSe_2/MoS_2 heterojunctions with three different twist angles: $\Delta\phi$ = (**d**) 7°, (**e**) 17°, and (**f**) 29°. M, MoS_2; W, WSe_2. Each kinetic profile can be described by a single exponential rise (CT process) and a single exponential decay (CR process), convoluted with the laser CC function. **g**, Interfacial charge transfer lifetime and charge recombination lifetime as a function of $\Delta\phi$ (bottom axis) or momentum change (top axis) in WSe2/MoS2 heterojunctions. Inset: scheme illustrating the twist angle in momentum space.

any clear correlation with the twist angle. Within each sample, we find that the CR kinetics is insensitive to the position within the heterojunction region.

The absence of correlation between CT/CR rates and $\Delta\phi$ is surprising, giving the large momentum change. One possibility of momentum conservation comes from the bound nature of intralayer and interlayer excitons. The amount of momentum change shown in Figure 3.3g is calculated based on the single particle picture. In reality, the reduced dielectric screening leads to

tightly bound intralayer and interlayer excitons in the WSe_2 monolayer and at the WSe_2/MoS_2 heterojunction, respectively. Our estimates based on the uncertainty principle and spatial localization of the excitons give uncertainties in parallel momentum of 0.15 and 0.08 $Å^{-1}$ for the WSe_2 monolayer and WSe_2/MoS_2 heterojunction, respectively;[65] these values are an order of magnitude too small to compensate momentum change accompanying the CT and CR processes.

Because the initial CT rate is orders of magnitude faster than the exciton trapping process in the WSe_2 monolayer, we do not need to consider the role of defects. Instead, we attribute the $\Delta\phi$ independent CT rates to the excess electron energy at type-II heterojunction, Figure 3.4a. The conduction band offset between WSe_2 and MoS_2 is large (0.76 eV).[67] The excess energy means that electron transfer process can sample a broader range of $K_{\parallel}$ space above CBM,[71] including the M point which intersects the K valley in WSe_2 at $\Delta\phi = 30°$. A recent ultrafast infrared spectroscopy study also suggests the presence of hot interlayer excitons at the heterojunction interface.[79] The large excess electronic energy in the interfacial CT process also accounts for the apparent temperature independence in the initial ultrafast CT rates (Figure 3.4b). The electron transfer event is followed by hot electron relaxation within the MoS_2 conduction band. The lowest energy direct gap nature at K valley in MoS_2 is well retained due to weak interlayer coupling.[66,67] After charge transfer, the electron is expected to relax to the K valley CBM in MoS_2 with the hole in the K valley CBM in WSe_2, forming an interlayer CT exciton.

Unlike the electron transfer process, the recombination between the electron at the MoS_2 CBM and the hole at the WSe_2 VBM occurs with well-defined momentum vectors and has to be accompanied by momentum change if they recombine directly. An electron-hole pair in a semiconductor or a semiconductor interface recombines via three likely channels: (i) radiatively,

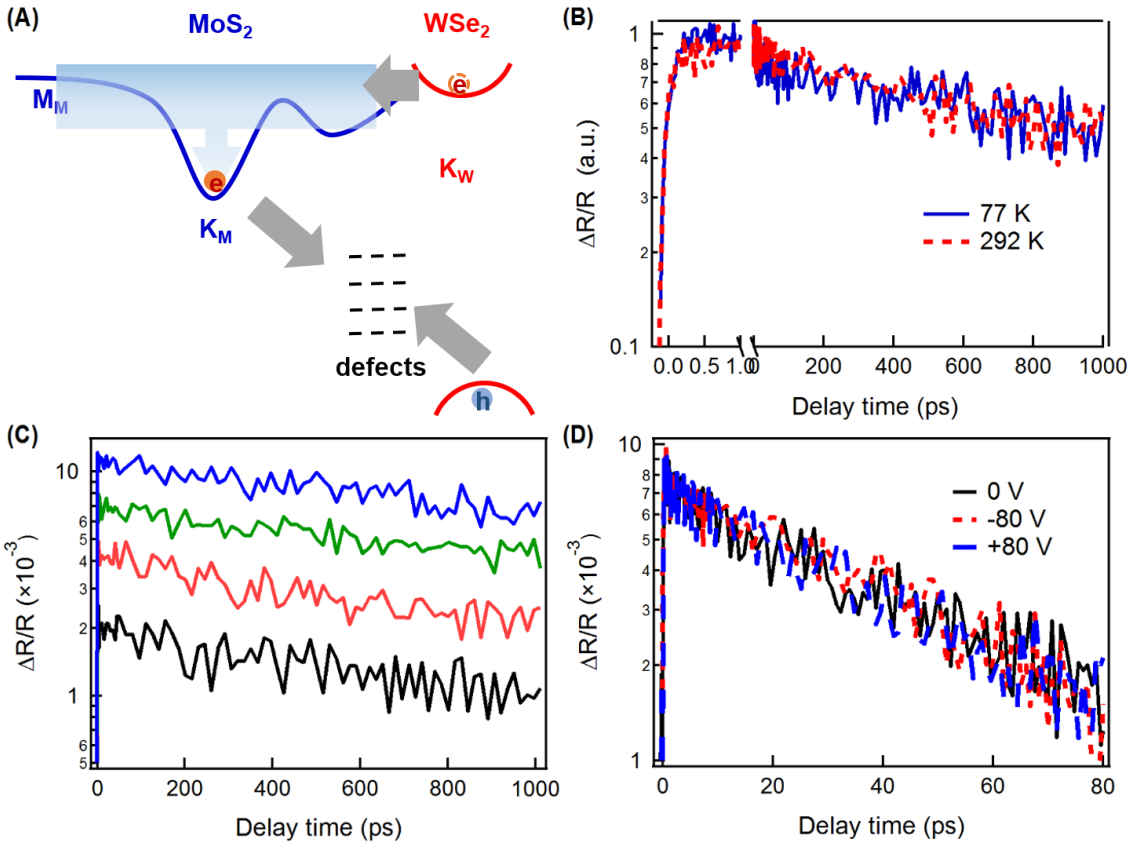

Figure 3.4 | Mechanism of twist angle independent carrier dynamics. a, Schematic illustration of interfacial charge transfer process at the WSe_2/MoS_2 heterojunction. After photoexcitation, electrons transfer from WSe_2 to MoS_2 with excess energy. After intra-band electron relaxation, interlayer electron−hole recombines through defect assisted non-radiative recombination. **b** and **c**, Electron population kinetics in MoS_2 layer for a representative sample at different temperatures (**b**, 77 and 292 K) and different excitation densities (**c**, from bottom to top 0.85, 1.7, 3.4, 5.1×10^{11} cm^{-2}). **d**, Charge recombination kinetics at different gating voltage which changes the doped electron density in the MoS_2 monolayer.

(ii) non-radiatively through Auger recombination, or (iii) non-radiatively via defect-assisted recombination. The radiative mechanism is not important here as CT exciton emission is not observed in our heterojunction samples. The Auger mechanism refers to the non-radiative recombination of the CT exciton with both energy and momentum transferred to another CT exciton or free carrier. Figure 3.4c shows CR kinetics of a representative heterojunction sample

as a function of excitation density. The independence of CR kinetics on excitation density precludes exciton-exciton Auger recombination in the excitation density range probed here ($\leq 5\times10^{11}$ cm^{-12}) in heterojunction. In contrast, we observe faster recombination for intralayer excitons in WSe_2 monolayer in the same excitation density. We also rule out exciton carrier based Auger scattering, as the CR dynamics is found to be independent of gate-doping of MoS_2, with either electron doping at V_g = +80 V or hole doping at V_g = −80 V, corresponding to electron and hole doping, respectively, of 6.2×10^{12} cm^{-2}, Figure 3.4d.

These results suggest that interlayer electron-hole recombination at the MoS_2/WSe_2 heterojunction is dominated by defect-assisted non-radiative electron-hole recombination, also known as the Shockley-Read-Hall mechanism.[80,81] Previous studies on TMDC monolayers have shown the detrimental role of defects on carrier dynamics and photoluminescence efficiencies.[73,75,82] The tightly localized nature of trapped carriers in defects can satisfy the momentum conservation for both carrier trapping and recombination with energy likely released through multi-phonon emission process. The properties of defect, including energetics, distributions, and densities, can vary from sample to sample, leading to large variations in interlayer CT exciton recombination rates. Thus, in order to probe the intrinsic physics of momentum conservation in radiative CT exciton emission, one must not only control the interlayer angular alignment within the range defined by the light cones[39,49] but also minimize trap densities at the TMDC heterojunction. The nature of these defects, how they exactly assist interlayer exciton recombination and how we may control them remain challenging questions that deserve answers in future experiments.

3.4 Conclusion

In summary, our findings suggest the following mechanisms for photo-induced charge separation and recombination at 2D TMDC heterojunctions with type II band alignment. Intralayer excitons from photoexcitation are dissociated with ultrafast rates and near unity yield by resonant interfacial charge transfer with injected charges carrying excess kinetic energy. After cooling to the band edges (K valleys), the interlayer CT exciton recombines non-radiatively through defect assisted recombination. The initial interfacial charge separation and the subsequent interfacial charge recombination circumvent momentum mismatch via excess electronic energy and via defects, respectively.

Chapter 4

Mott Transition in $MoSe_2/WSe_2$ Heterobilayers: Spectroscopy*

Controlling charge density in 2D materials is a powerful approach for engineering new electronic phases and properties. This control is traditionally realized by electrostatic gating. In this chapter, we report an optical approach for generation of high carrier densities using transition metal dichalcogenide heterobilayers, $MoSe_2/WSe_2$ with type-II band alignment. By tuning the optical excitation density above the Mott threshold, we realize the phase transition from interlayer excitons to charge-separated electron/hole plasmas, where photoexcited electrons and holes are localized to individual layers. High carrier densities up to 4×10^{14} cm^{-2} can be sustained under both pulsed and continuous wave excitation conditions. These findings open the door to optical control of electronic phases in 2D heterobilayers.

4.1 Introduction

2D TMDCs are emerging platforms for exploring a broad range of electronic, optoelectronic, and quantum phenomena. These materials feature strong Coulombic interactions, making them ideal for studying highly correlated quantum phenomena as a function of charge-carrier density. Seminal demonstrations include among others, charge-density waves and superconductivity in $TiSe_2$ and MoS_2 by electrostatic gating [83–86]. These exciting demonstrations have been possible due to the high charge carrier densities (~10^{14} cm^{-2}) achievable with ionic

* This chapter is based on work published[103]: *Science Advances* **5**, eaax0145 (2019).

liquid gating. Under bias, a capacitive electrical bilayer is formed between the charge carriers in the 2D material and counter ions in the liquid. Among the limitations of using a liquid as dielectric is that controlling charge carrier density requires gate switching near room temperature, but the appearance of interesting electronic phases occurs mostly upon cooling on hour time scales under the gate bias.

Alternatively, in TMDC type-II hetero-bilayers, photo-excited electrons and holes separate on femtosecond time scales [36,87] to form oppositely charged monolayers. While these spatially separated electrons and holes form Coulomb bound interlayer excitons[42,45,50,88], the insulating exciton gas can be transformed to conducting charge-separated electron/hole (e/h) plasmas if excitation density is increased to above the Mott threshold (n_{Mott}) [89,90], as illustrated schematically at the top of Figure 4.1 for the $WSe_2/MoSe_2$ hetero-bilayer studied here. The Mott transition has been observed in optically excited monolayer and bilayer WS_2[29], but the electron and hole plasma exist in the same material which remains charge neutral. In contrast, TMDC hetero-bilayers host spatially separated electron/holes with long lifetimes[42,44,45,50,88]. Therefore, these systems offer a unique opportunity to control high carrier densities in individual 2D monolayers. In this case, the resulting e/h bilayer across the hetero-interface in the presence of photo-excitation, particularly under CW conditions, resembles the capacitive electric bilayer in an ionic gated 2D material. Here we use photoluminescence (PL) spectroscopy and time-resolved reflectance spectroscopy to demonstrate optically driven Mott transition from interlayer exciton to charge-separated electron/hole plasmas in the $WSe_2/MoSe_2$ hetero-bilayer. The experimental findings are supported by calculations from quantum theory. The achieved carrier density is as high as $4x10^{14}$ cm^{-2}, more than two orders of magnitude above the Mott density.

4.2 Photoluminescence spectroscopy

We use transfer stacking to form $WSe_2/MoSe_2$ hetero-bilayers encapsulated by hexagonal boron nitride (h-BN), with the two TMDC monolayers aligned within the light-cone [39] for radiative interlayer exciton emission (twist angle $\theta = 4\pm2^o$ from K/K or K/K' stacking), with a dark hetero-bilayer sample with $\theta = 13\pm2^o$ (from K/K or K/K' stacking) as control. The WSe_2 and $MoSe_2$ monolayers are exfoliated from flux-grown single crystals, each with defect density < 10^{11} cm^{-2}, two orders of magnitude lower than in commonly used commercial crystals [13]. This is critical for suppressing defect-mediated non-radiative recombination previously seen to dominate TMDC hetero-bilayers [87] and for sustaining high excitation density in the charge separated electron/hole plasmas. All measurements are carried out with the samples at 4 K in a liquid helium cryostat. The spectroscopic measurements include steady-state PL with continuous wave (CW) excitation (2.33 eV), time-resolved (TR) PL with pulsed excitation (2.33 eV, pulse width 150 fs), transient reflectance spectroscopies with pulsed excitation (1.82 eV, pulse duration 150 fs). At both excitation photon energies, we calculate the absorptance (percentage of incident light absorbed) to be 8% at the low excitation density limit, based on the reported dielectric functions of WSe_2 and MoS_2 monolayers [57]. We carefully calibrate experimental electron/hole density, n_{eh}, by including saturation of absorptance from self-consistent Maxwell-semiconductor Bloch equation calculations. Under the experimental conditions employed here, we find the measurements completely reproducible, i.e., there is no sample damage due to laser excitation. However, damage to other heterobilayer samples have been observed for laser excitation exceeding the upper limit shown here.

Figure 4.1a shows CW PL spectra from the $WSe_2/MoSe_2$ hetero-bilayer with n_{eh} spanning over four orders of magnitude (1.6×10^{10} to 3.2×10^{14} cm^{-2}), achieved by varying excitation power

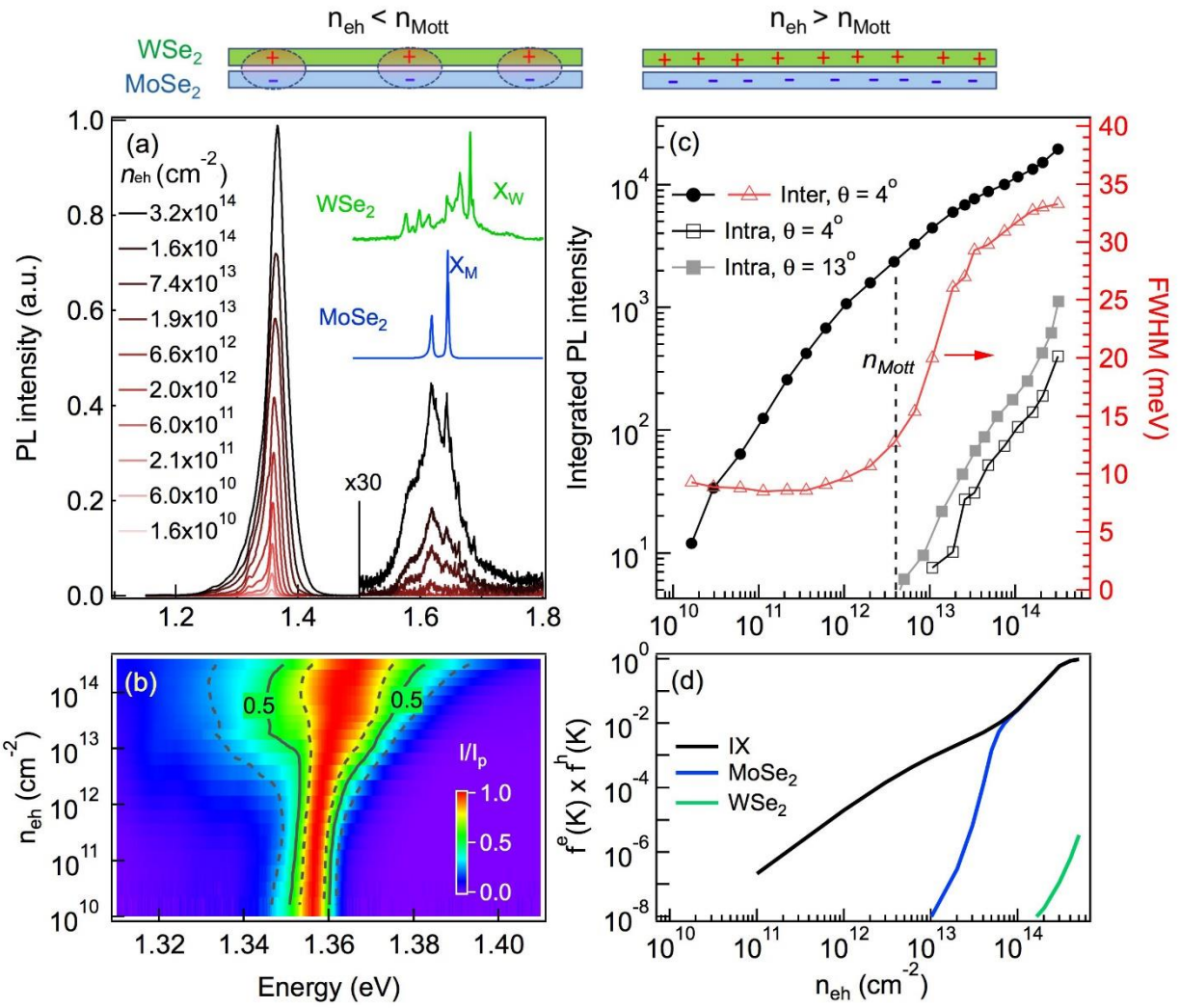

Figure 4.1 | Excitation density dependent PL and Mott transition in $MoSe_2/WSe_2$ heterobilayers. **a** and **b**, PL spectra (**a**) and intensity-normalized PL spectra (**b**) from a BN-encapsulated $MoSe_2/WSe_2$ heterobilayer with $\theta = 4° \pm 2°$. a.u., arbitrary units. The spectral region ($h\nu \geq 1.51$ eV) corresponding to intralayer PL is multiplied by a factor of 30. Also in (**a**) is PL from monolayer WSe2 (green) and monolayer MoSe2 (blue). Shown in (**b**) are contours of 50% (solid curve) and 25 and 75% (dashed curves) of peak intensity. **c**, Integrated intensities (left axis) of interlayer (1.2 to 1.5 eV, solid black circles) and intralayer (1.51 to 1.80 eV, open black squares) PL emission, FWHM of the interlayer exciton peak (open red triangles, right axis) as a function of n_{eh}, and integrated intralayer PL intensities (solid gray squares) from a BN-encapsulated $MoSe_2/WSe_2$ heterobilayer with $\theta = 13° \pm 2°$. **d**, Computed joint electron/hole populations in the K valleys for interlayer exciton (black) and intralayer excitons in $MoSe_2$ (blue) and WSe_2 (green). The top of the figure is a cartoon illustrating the Mott transition in the $MoSe_2/WSe_2$ heterobilayer.

density from 0.5 W/cm^2 to 1.5×10^5 W/cm^2. We quantitatively calibrate the equilibrium excitation density based on $n_{eh} = F \cdot \sigma \cdot \tau_0$, where F is the incident photon flux, σ is the absorptance, and τ_0 is the population decay time constant determined in TR-PL; both σ and τ_0 are numerical functions of n_{eh} (see below) determined systematically through our computations and measurements, respectively. A complete set of spectra with normalized peak intensities is shown for the 1.31-1.41 eV region in Figure 4.1b. Also shown in Figure 4.1a are PL spectra of $MoSe_2$ (blue) and WSe_2 (green) monolayers. The former is characterized by the neutral exciton (X_M) and the trion while the latter consists of a series of peaks assigned to exciton (X_W), trion, biexciton, etc., in agreement with previous reports [15,17–19]. At $n_{eh} \leq 1\times10^{13}$ cm^{-2} in the hetero-bilayer, PL from intralayer excitons are completely quenched while interlayer exciton (IX) emission with E_{IX} = 1.3566±0.0005 eV (at $n_{eh} = 1.6\times10^{10}$ cm^{-2}) dominates [42,49]. The IX peak grows with n_{eh} and blue- shifts only by ~8 meV in the entire excitation density range, as is known for coupled [91] and uncoupled [92] III-V quantum wells.

To experimentally detect the Mott transtion, we plot in Figure 4.1c the n_{eh} dependences of the integrated intensities from interlayer PL (solid black circles) and its spectral full-width-at-half-maximum (FWHM, open red triangles) along with the intralayer PL (open black squares) integrated over the 1.5-1.75eV energy rage. The interlayer emission peak broadens substantially when the theory-assigned $n_{Mott} = 3\times10^{12}$ cm^{-2} (vertical dashed line, see below) is crossed. The corresponding FWHM increases by as much as a factor of four, verifying that excitons (and the narrow linewidth they sustain) are absent above n_{Mott}. We also observe that intralayer PL, corresponding to broad emission from $MoSe_2$ and/or WSe_2 monolayer(s), reappears and grows for $n_{eh} > 1\times10^{13}$ cm^{-2}. As the charge-separated e/h plasmas form at $n_{eh} > n_{Mott}$, the band offsets between the two TMDC monolayers are reduced due to both band-renormalization and charge

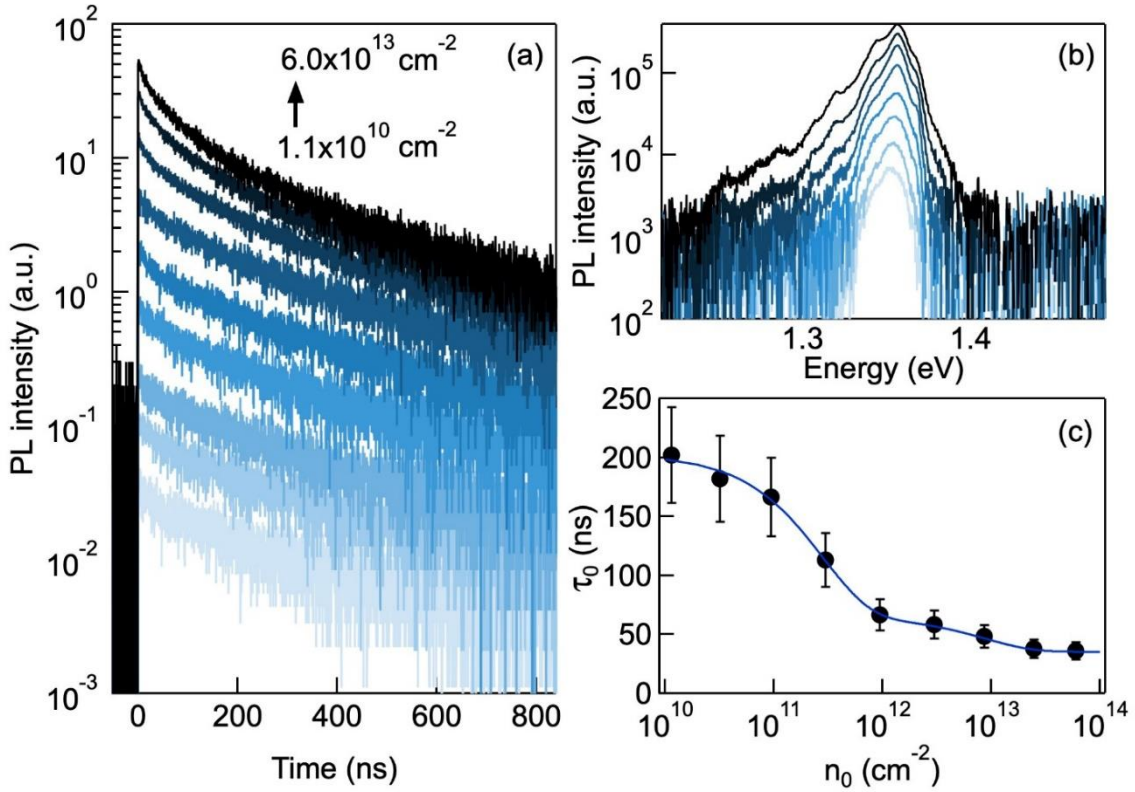

Figure 4.2 | Time-resolved photoluminescence of interlayer excitons in the $MoSe_2/WSe_2$ heterobilayer. The sample at 4 K is excited by pulsed laser ($h\nu$ = 2.33 eV; pulse duration, 150 fs). **a**, The energy-integrated emission from the interlayer exciton is detected as a function of time for initial excitation densities of (from bottom to top) $n_0 = 1.1\times10^{10}$, 3.0×10^{10}, 9.4×10^{10}, 3.0×10^{11}, 9.4×10^{11}, 3.0×10^{12}, 8.7×10^{12}, 2.5×10^{13}, and 6.0×10^{13} cm^{-2}. **b**, PL spectra at the same pulsed excitation densities as **a**. **c**, Initial decay time constants (solid circles) as a function of n_0. The solid line is the bi-exponential fit to the data.

separation. The latter can be understood from a simple capacitive model which predicts from the e/h charge separation a voltage buildup, ΔV_C. This ΔV_C can cancel out the initial ~300 meV band offset [44], leading to the repopulation of the conduction (valence) band of WSe_2 ($MoSe_2$) and to intralayer radiative recombination. This interpretation is supported theoretically, Figure 4.1d, which shows the computed source for PL emission, i.e. the probability of simultaneously finding electrons and holes in the K valleys of WSe_2 (green), $MoSe_2$ (blue), and between the two

monolayers (black). The experimental onset of intralayer PL matches perfectly with the rise in the computed spontaneous emission source for $MoSe_2$, while PL from WSe_2 remains suppressed. Further support for this interpretation comes from PL measurement on the control sample of a $WSe_2/MoSe_2$ hetero-bilayer with $\theta = 13\pm2^o$ alignment. The large momentum mismatch between the K or $-K$ valleys across the interface means that the interlayer excitons are non-radiative [88]. Indeed, we observe no measurable IX emission, but only intralayer PL at $n_{eh} >> n_{Mott}$ (solid grey squares in Figure 4.1c).

We determine the lifetimes of interlayer exciton emission using TRPL under pulsed excitation (2.33 eV). Figure 4.2a shows TRPL data in the broad initial excitation density range of $n_0 = 1.1\times10^{10} - 6.0\times10^{13}$ cm^{-2}. The corresponding time-integrated PL spectra, Figure 4.2b, are similar to the CW PL spectra in Figure 4.1a. The PL decays at low excitation densities ($10^{10\text{-}11}$ cm^{-2}) are close to single exponentials, with decay time constant of $\tau_0 = 200\pm40$ ns. As n_0 increases, particularly above n_{Mott}, the PL decay becomes faster and exhibits a major deviation from single exponential. This behavior is expected for plasma luminescence, as demonstrated in various III-V quantum well systems [93]. Above the Mott transition, luminescence from the e/h plasma scales approximately with n_{eh}^2. Additionally, carrier density may decay non-radiatively, e.g., via Auger recombination that scales approximately with n_{eh}^3. As a result, PL decays faster at higher carrier densities, but this is difficult to analyze quantitatively due to the varying Auger scattering cross section resulting from the expected density-dependent Coulomb screening. Figure 4.2c plots the initial PL decay time constant as a function of n_0. Our PL lifetimes are one-two orders of magnitude longer than those of previous reports on $WSe_2/MoSe_2$ hetero-bilayers [42,49,94], suggesting the suppression of non-radiative recombination in the less defective TMDC samples used here. These long PL lifetimes are essential to reaching excitation density well

above the Mott threshold and to obtaining high equilibrium n_{eh} under CW excitation, as n_{eh} is proportional to τ_0.

4.3 Transient reflectance

To further explore the properties of charge separated e/h plasmas in the $WSe_2/MoSe_2$ hetero-bilayer, we apply transient reflectance spectroscopy (time resolution ~40 fs) which has been used before to probe excitons and e-h plasma in TMDC monolayers [29] and charge separation in hetero-bilayers [36,87]. We excite the samples with a 150 fs pulse at 1.82 eV and probe the change in reflectance using broadband white light (1.2 – 1.8 eV). We present transient reflectance, $\Delta R/R_0$, as a function of pump-probe delay (Δt), where $\Delta R = R - R_0$; R is the reflectance at Δt and R_0 is the reflectance without the pump. At the 2D limit and low excitation densities, $\Delta R/R_0$ is proportional to transient absorption [30]. Figures 4.3a-d show pseudo-color plots of transient reflectance spectra in a broad range of excitation densities. At $n_0 \leq n_{Mott}$, Figure 4.3a or 3b, each spectrum is dominated by two prominent photo-bleaching peaks at ~1.62 eV and ~1.70 eV, attributed to reduction of oscillator strength [87] of transitions in monolayer WSe_2 and $MoSe_2$, respectively. The induced absorption signal (red) on the sides of the main bleaching peaks can be attributed to shifts in intralayer transition energies resulting from competing effects of screening/Pauli blocking of the Coulomb interaction and band renormalization. Note that, at $n_0 < n_{Mott}$, $\Delta R/R_0$ is negligible below 1.5 eV, including the IX region. This is expected as the oscillator strength of interlayer exciton is two orders of magnitude lower than those of intralayer excitons in each monolayer [43]. The absence of $\Delta R/R_0$ signal below 1.5 eV is evident in horizontal cuts at selected Δt values, shown for $n_0 = 1\times10^{11}$ cm^{-2} in Figure 4.3e.

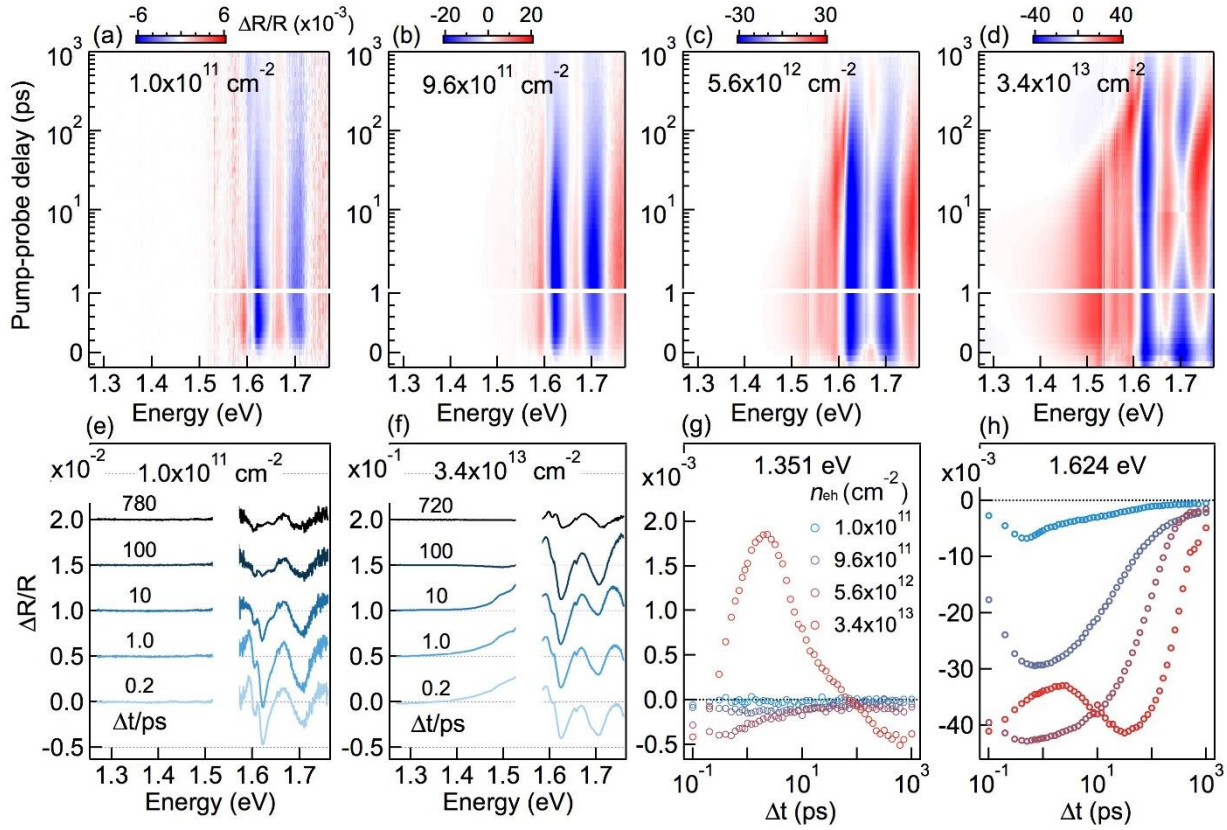

Figure 4.3 | Density-dependent transient reflectance spectra from the $MoSe_2/WSe_2$ heterobilayer. The $WSe_2/MoSe_2$ heterobilayer was excited at $h\nu$ = 1.82 eV with initial excitation densities of n_0 = (**a**) 1.0×10^{11}, (**b**) 9.6×10^{11}, (**c**) 5.6×10^{12}, and (**d**) 3.4×10^{13} cm^{-2} at a sample temperature of 4 K. The excited sample is probed with a white light, and the pseudocolor scale is $\Delta R/R_0$ (blue , bleaching; red, induced absorption). Transient reflectance spectra at selected pump-probe delays (Δt) at n_0 = (**e**) 1.0×10^{11} and (**f**) 3.4×10^{13} cm^{-2} are also shown. The probe regions around 1.55 eV are blocked out due to low intensity and noise from white light which was generated by 1.55 eV laser light. Kinetic profiles obtained from vertical cuts at (**g**) 1.351 and (**h**) 1.624 eV in the 2D pseudocolor plots at the four n_0 values.

In agreement with the CW results in Figure 4.1a, transient reflectance spectra under pulsed excitation reveal plasma formation above the Mott density. At $n_0 = 5.6\times10^{12}$ or 3.4×10^{13} cm^{-2} (Figure 4.3c and d), the spectra show, in addition to bleaching of intralayer exciton transitions, broad induced absorption extending to the low energy end (~1.3 eV) of the probe window. These broad features are evident in horizontal cuts (spectra) at short pump-probe

delays, as shown for $n_0 = 3.4\times10^{13}$ cm^{-2} in Figure 4.3f. This broad absorption feature is optical signature of a 2D plasma, which consists of broad induced absorption (positive) extending to the renormalized band gap and gain (negative) just above the band gap [29,95].

4.4 Theory of optical response of interlayer exciton and charge separated plasmas

To calculate the optical properties of photoexcited transition metal dichalcogenide (TMDC) hetero-bilayers, we solve the semiconductor Bloch equations (SBE) [11,96] for the microscopic inter-band polarizations $\psi_k^{he}(t)$

$$i\hbar\frac{d}{dt}\psi_k^{he}(t) = \left(\varepsilon_{k,0}^{e} + \varepsilon_{k,0}^{h} + \Sigma_{k,SXCH}^{e} + \Sigma_{k,SXCH}^{h}\right)\psi_k^{he}(t)$$

$$-\left(1 - f_k^e - f_k^h\right)\left(d_k^{eh}E(t) + \sum_{k\prime} W_{k,k\prime}^{eh}\,\psi_{k\prime}^{he}(t)\right)$$

with a weak external probe field $E(t)$ incident perpendicular on the TMDC hetero-bilayer. The photoexcited electrons and holes generated by a strong pump field are described in quasi-equilibrium by Fermi distribution functions f_k^a. The linear susceptibility

$$\chi(\omega) = \sum_{k,eh} \psi_k^{he}(\omega)\, d_k^{eh}/E(\omega)$$

in the frequency domain is used in a second step to derive reflectance and absorptance spectra, as detailed below.

In the SBE, material properties enter via band structures ε_k^a, screened Coulomb matrix elements W_q and dipole matrix elements d_k. Band structure renormalizations due to photoexcited carriers are given by the screened-exchange-Coulomb-hole self-energy $\Sigma_{k,SXCH}^a$, while plasma screening is described by a dielectric function in the long-wavelength approximation via $W_{k,k\prime}^{ab} = \varepsilon_{k-k\prime,pl}^{-1} V_{k,k\prime}^{ab}$ [96]. The band structure of the unexcited $MoSe_2/WSe_2$ heterobilayer is modeled under

an effective-mass approximation for the relevant conduction- and valence-band valleys. The energetic ordering of the bands is inspired by first-principle calculations [44], while we adjust the band edges to match our experimental reflectance spectra. We assume that the effective masses are approximately given by the masses of the respective monolayers as provided in ref. [8]. For the Q- and Γ-valleys we average over both materials.

The Coulomb interaction between carriers located in different TMD layers is significantly weaker than intra-layer Coulomb interaction due to the spatial separation of carriers in growth direction. To account for this effect, we use model Coulomb matrix elements in a two-dimensional layer basis $|\alpha\rangle = \{|\mathrm{MoSe_2}\rangle, |\mathrm{WSe_2}\rangle\}$:

$$V_{k,k}^{ab} = \sum_{\alpha,\beta} \bar{c_\alpha^a}(k)\bar{c_\beta^b}(k')c_\beta^b(k)c_\alpha^a(k')V_{k-k'}^{\alpha\beta},$$

where the contribution of a certain layer α to the band a is given by $|c_\alpha^a(k)|^2$. We assign layer contributions according to the first principle results in ref. [44]. The matrix elements $V_q^{\alpha\beta}$ are modeled by a macroscopic dielectric function $\varepsilon_{q,b}^{-1,\alpha\beta}$ and a form factor $F_q^{\alpha\beta}$ according to

$$V_q^{\alpha\beta} = \frac{e^2}{2\varepsilon_0 q}\varepsilon_{q,b}^{-1,\alpha\beta}F_q^{\alpha\beta}$$

The dielectric function for each layer combination is obtained by solving Poisson's equation for the respective dielectric structure [97]. The dielectric constants of the TMD materials are computed as geometric mean of the values given in ref. [98], where also layer widths are provided. The dielectric constant of hBN is taken from ref. [99]. The layer-substrate distance h_1=0.5 nm has been found to be an appropriate value in ref. [97], while we assume that the two TMD layers are slightly closer to each other using h_2=0.3 nm. The form factor accounts for the confinement of carriers inside the atomically thin layers via the confinement functions $\xi^\alpha(z)$:

$$F_q^{\alpha\beta} = \int dz \int dz' \xi^\alpha(z)\xi^\beta(z')e^{-q|z-z'|}\xi^\beta(z')\xi^\alpha(z).$$

For the confinement functions, we assume eigenfunctions of the infinitely deep potential well with two nodes due to the mostly d-like character of electronic orbitals.

To describe light-matter interaction, we assume a circularly polarized electric field selecting dipoles in the K-valley between like-spin bands. The numerical values for the intra-layer dipoles are computed using the simple lattice model from ref. [5], where we neglect the momentum dependence. For the inter-layer transition dipoles, we assume a value that is 10 times smaller than that in the $MoSe_2$ monolayer [43].

The SBE contains a phenomenological damping factor γ, which corresponds to the HWHM of lines in optical spectra. Due to excitation-induced dephasing, γ depends on the actual excited-carrier density. We fix the value of γ at different densities by matching simulated and experimental reflectance spectra. For the intra-layer $MoSe_2$ transition, this yields γ=25 meV for carrier density $n = 1.3\times10^{12}$ cm^{-2}, γ = 30 meV for $n = 1.9\times10^{12}$ cm^{-2}, γ = 35 meV for $n = 5.3\times10^{12}$ cm^{-2} and γ = 50 meV for $n = 3.13\times10^{13}$ cm^{-2}. For the intra-layer WSe_2 transition, we use a γ that is 50% larger to account for the stronger dephasing, in accordance with the experimental reflectance spectra.

Figure 4.4a shows simulated transient reflectance spectra at excitation densities n_0 = 6×10^{11}, 4×10^{12}, and 3×10^{13} cm^{-2}, obtained from theoretical optical absorptance and the experimental sample geometry. Also shown as comparison are experimental transient reflectance spectra (Δt = 1 ps) at similar n_0 values, Figure 4.4b. The simulations and experimental spectra are in excellent agreement, including main features of bleaching of intralayer excitonic transitions for all excitation densities, the broad induced absorption feature above the Mott density, and stimulated emission near the renormalized bandgap at ~1.3 eV. This agreement provides strong support for the conclusion on Mott transition from the interlayer exciton to

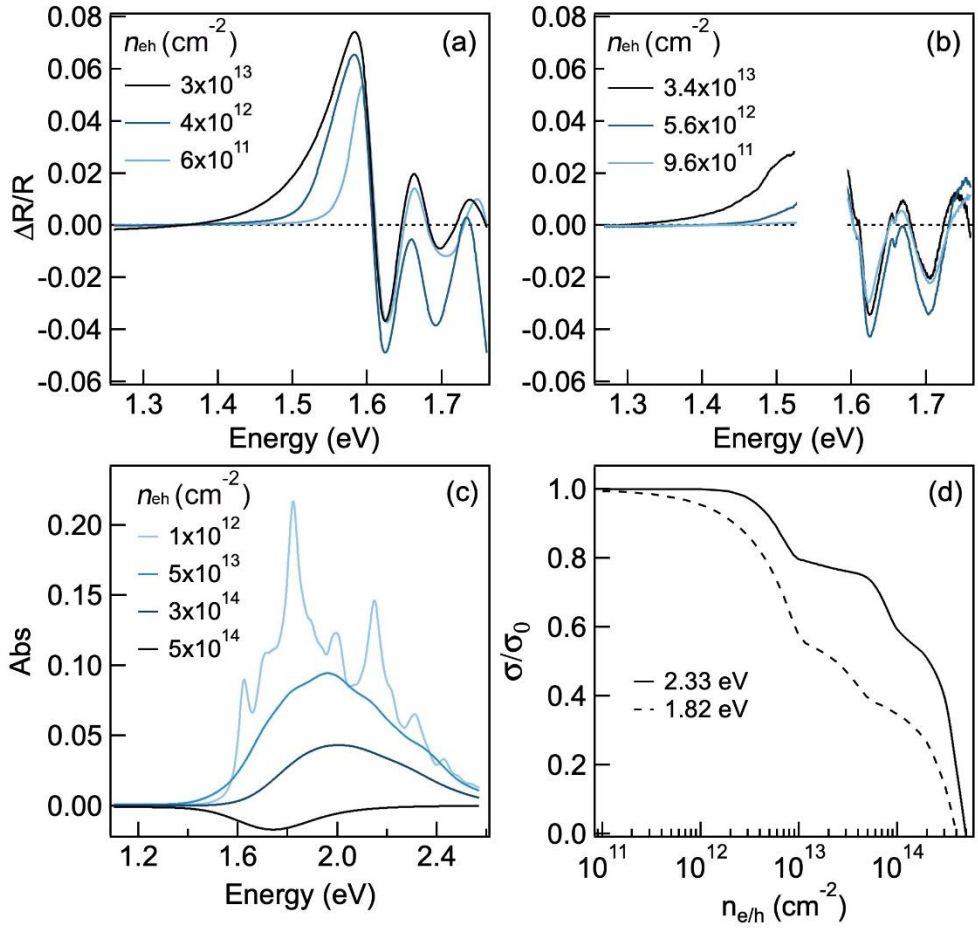

Figure 4.4 | Calculated optical spectra of the $MoSe_2/WSe_2$ heterobilayer. a, Simulated reflectance spectra from theoretical optical spectra and experimental sample geometry at the indicated excitation densities (n_{eh} = 6×10^{11} to 3×10^{13} cm^{-2}). **b**, Experimental reflectance spectra at Δt = 1 ps at initial excitation densities of n_0 = 9.6×10^{11} to 3.4×10^{13} cm^{-2}. **c**, Calculated optical absorptance spectra at n_{eh} = 1×10^{11} to 5×10^{14} cm^{-2}. **d**, Calculated relative optical absorptance as a function of n_{eh} at two photon energies used in the experiments.

charge separated e/h plasma, as well as for the calibration of carrier density in the CW measurement in Figure 4.1.

Figure 4.4c show calculated absorptance spectra at selected n_{eh} values. By determining at which n_{eh} excitonic absorption resonance becomes bleached, we find n_{Mott} = 3×10^{12} cm^{-2}. This value is close to n_{Mott} = 1.6×10^{12} cm^{-2} obtained from an analytical estimate[95] of $a_0 {n_{Mott}}^{1/2} \approx$

0.25 and an interlayer exciton radius of ~2 nm [44]. More specifically, we follow excitonic absorption where exciton features gradually fade through broadening from a clear peak to transparency and eventually to gain [92,100]. Below n_{Mott}, the presence of excitons significantly reduces scattering. There is an accelerated broadening after excitons cease to exist above n_{Mott} [92] and this leaves a signature in increased PL linewidth. Note that the observed increase in PL peak width above the Mott density is much larger than what was observed before in coupled III-V quantum wells[89,90]. The inter-layer excitons in the 2D TMDC hetero-bilayer[42,45,50,88] is much more strongly bound and less Coulomb screened than their counter parts in III-V coupled quantum wells[89,90]; as a result, the Mott transition has a much larger effect on reducing Coulomb screening in the former.

In addition to revealing the Mott threshold from the disappearance of sharp excitonic features, the theoretical absorption spectra show the decrease in oscillator strength with increasing n_{eh}, as expected from Pauli blocking and screening effects. Optical transparency is reached at $n_{eh} \sim 4\times10^{14}$ cm^{-2} above which stimulated emission dominates. Based on the calculated optical spectra, we obtain the n_{eh}-dependent relative absorptance (σ/σ_0, where σ_0 is the absorptance at the low n_{eh} limit) shown in Figure 4.4d for two photon energies. These calculated results are used in the calibration of experimental excitation densities.

4.5 Discussion and conclusion

We now turn to the mechanism of PL emission from interlayer excitons and charge separated e/h plasmas. A comparison of TRPL in Figure 4.2 and transient reflectance in Figure 4.3 reveals a major discrepancy in the time scales involved. PL decays are characterized by time constants of ~10^2 ns, but transient reflectance features time constants in the range of $10^{1\text{-}2}$ ps. We show kinetic profiles (vertical cuts of transient reflectance spectra) for two representative probe

energies, $h\nu$ = 1.351 eV and 1.624 eV for induced absorption (Figure 4.3g) and photo-bleaching (Figure 4.3h), respectively. Figure 4.3g shows little induced absorption at $h\nu$ = 1.351 eV, for n_0 = 1×10^{11} cm^{-2} and 9.6×10^{11} cm^{-2}, as expected from the absence of plasmas. When n_0 is increased above n_{Mott}, we observe both positive (induced absorption) and negative (stimulated emission) $\Delta R/R_0$ signal, consistent with the transformation to the charge separated plasma region. For the intermediate density $n_0 = 5.6\times10^{12}$ cm^{-2}, stimulated emission dominates. At the highest density of $n_0 = 3.4\times10^{13}$ cm^{-2}, induced absorption dominates at Δt < 60 ps and stimulated emission at Δt > 60 ps.

The kinetics profiles at $h\nu$ = 1.624 eV, Figure 4.3h, reveal the short time nature of photo-bleaching. At $n_0 = 1.0\times10^{11}$, 9.6×10^{11}, and 5.6×10^{12} cm^{-2}, photo-bleaching ($-\Delta R/R_0$) grows with time constants of τ_1 = 140±30 fs, attributed to the ultrafast dissociation of intralayer excitons in each TMDC monolayer to form charge separated states that increase the Pauli blocking effect. The photo-bleaching intensity peaks in sub-picoseconds and decays on longer time scales. At $n_0 \leq n_{Mott}$ (1.0×10^{11} cm^{-2} and 9.6×10^{11} cm^{-2}), bleaching intensity decays with time constants of τ_2 = 30±10 ps. This time constant increases above n_{Mott} to τ_2 = 90±30 ps and τ_2 = 290±60 ps at n_0 = 5.6×10^{12} cm^{-2} and 3.4×10^{13} cm^{-2}, respectively. There is a three-order of magnitude difference between the time constants for PL decay (τ_{PL}) and those of photo-bleaching recovery (τ_2). The fast recovery in photo-bleaching cannot result from the loss of photo-excited charge carriers to recombination, but rather to the scattering of these carriers away from the K valley. Computational studies on the $WSe_2/MoSe_2$ hetero-bilayer have shown that the conduction band is lower in energy at the Q point than that at the K point, while valence band energy at the Γ point is close in energy to that of the K point [44]. Following charge separation, inter-valley scattering transfers carrier populations in the K valleys to the Q and Γ valleys. This process

reduces Pauli blocking of optical transitions in the K valleys and accounts for the τ_2 = 30-290 ps decay time constants. Efficient intervalley carrier scattering involves optical phonons and its rate is decreased by screening as excitation density is increased, thus accounting for longer τ_2 at higher n_0 above n_{Mott}. The Q and Γ valleys serve as carrier reservoirs; the momentum-indirect nature prohibits radiative recombination of electrons and holes in these valleys. Instead, scattering of electrons and holes back to the K valleys likely occurs before radiative recombination happens. This explains the long PL lifetimes on the 10^2 ns timescale. In a similar proposal, dark traps have been suggested as exciton reservoirs for slow PL emission in monolayer MoS_2 [101].

The results presented here establish photo-induced charge separation at van der Waals interfaces as an effective means to control 2D charge carrier densities. Using the hetero-bilayer of $WSe_2/MoSe_2$, we show spectroscopic signature of Mott transition from interlayer excitons to charge separated electron/hole plasmas, in excellent agreement with calculation based on a fully microscopic quantum theory. We point out that the spectroscopy measurements probe the combined responses of the electron plasma and hole plasma across the hetero-bilayer interface. Resolving the individual response of the electron or hole plasma is challenging, but possible with time-resolved and angle-resolved photoemission spectroscopy (TR-ARPES), which is underway in our laboratory[32]. The combined photoluminescence and transient reflectance measurements also reveal the participation of intervalley scattering and dark exciton/carrier reservoirs in radiative recombination dynamics. Remarkable, photo-induced charge separation under CW conditions allows us to reach charge carrier densities as high as ~4×10^{14} cm^{-2}, which is two orders of magnitude above the Mott density and is at the same level demonstrated previously for gate-doped superconductivity in TMDCs [83–86]. These findings suggest that photo-induced charge

separation at van der Waals interfaces is an effective means to realize complex electronic phases in 2D materials, particularly photo-induced superconductivity under CW conditions.

This page intentionally left blank

Chapter 5

Mott Transition in $MoSe_2/WSe_2$ Heterobilayers: Transport

The physics of Mott transition, i.e. the transition between metal and insulator states of a matter where the relative strength of kinetic and potential energy is varied, lies in the core of condensed matter physics. The interplay between kinetic hopping and Coulomb correlation, tunable by carrier filling, lattice spacing, temperature and other variables, was known to produce a whole spectrum of electronic phases even in the simplest Mott-Hubbard model. 2D materials, with intrinsic poorly screened Coulomb interaction, is revealing its potential in conceiving series of exotic electronic phases. On top of that, the 2D heterostructures, assembly of 2D monolayers by van der Waal force, offer extra versatility in tuning electronic band structure such as stacking order, twist angle and atomic registry. Reducing the electron kinetic energy by twisting to the magic angle, the correlated insulating and superconducting states were recently achieved in graphene bilayers at finite doping and ground state[34,35].

The electron hole system in photo-excited semiconductors is another ideal platform for the Mott physics[102]. Here the photo-injected electrons and holes, in a quasi-equilibrium or stead-state, are subject to Coulomb attraction resulting in bound pairs at low temperature and low carrier density, namely excitons. 2D semiconductors, especially transition metal dichalcogenides (TMDC), have been shown to have large exciton binding energy and impressive Mott transition between exciton and electron-hole plasma phases[29,32]. However, the strong Coulomb interaction also limits the lifetime to less than 10 ps therefore constrain Mott transition to ultrafast time scale and pulsed excitation conditions. 2D TMDC heterobilayers inherit the strong Coulomb correlation; meanwhile the efficient spatial separation of electrons and holes into different layers

due to type-II band alignment reduces electron-hole scattering cross section and significantly elongates the lifetime[36,38,42,87,103], making them promising candidates for achieving exciton condensation[51–53] as well as valleytronics[49,50,88,104] and moiré topological excitons[40,105–107]. While the interlayer exciton phase received most of the attention, little is explored of other electronic phases and phase transitions in 2D TMDC heterobilayers, especially the fundamental Mott transition between insulating interlayer exciton or exciton condensate states and conducting or superconducting metallic states.

Here we use various types of transport and spectroscopic techniques to directly probe this insulator metal transition of the interlayer electron hole system in 2D $MoSe_2/WSe_2$ heterobilayers. As was previously demonstrated, a carrier lifetime on the order of 10^2 ns is essential for maintaining high carrier densities up to ~0.4 pairs of electron and hole per unit cell under steady-state optical excitation, as can be seen in the steady-state condition $n=G(n)t(n)$, where $n=n_e=n_h$, G and t are the density, generation rate and decay rate of electron hole pairs[103]. To this end, we used high quality exfoliated monolayers with very low ($<10^{11}$ cm^{-2}) defect density[13] and BN encapsulation technique[12] in fabricating $MoSe_2/WSe_2$ heterostructures. All measurement was done at 4 K to reduce possible scattering pathways and obtain intrinsic properties of the electron hole system.

5.1 Photoconductivity

First we measure the conductivity of interlayer electron hole system at different steady-state carrier densities. A continuous wave laser (2.33 eV) was used to evenly illuminate the heterobilayer as well as the contact to graphene electrodes. A steady state forms from balanced generation and decay of interlayer electron hole pairs, making it possible to measure the electrical transport by simply biasing a low frequency AC current and measure the voltage drop

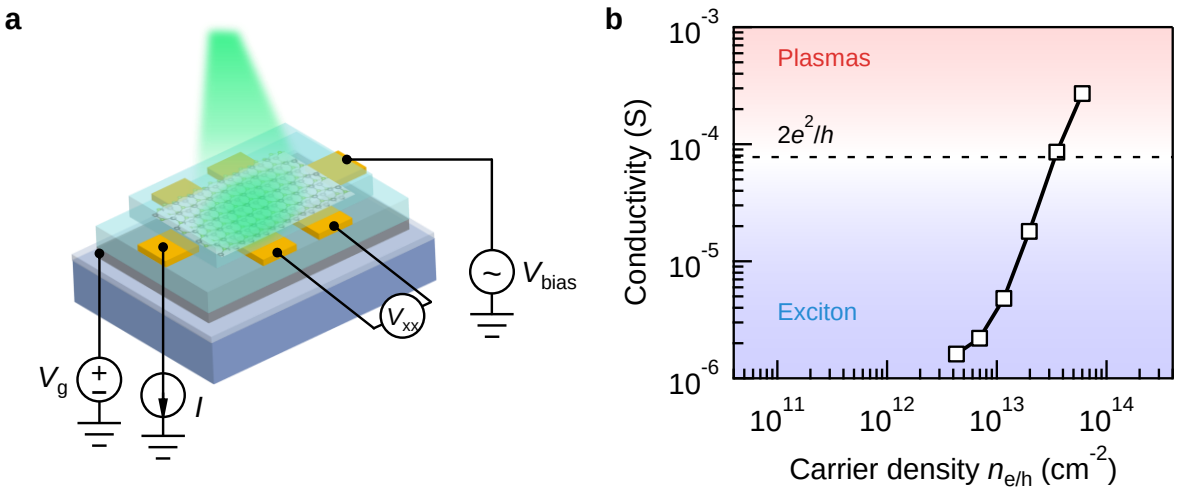

Figure 5.1 | Photoconductivity of $MoSe_2/WSe_2$ heterobilayer. a, Schematics of four-terminal conductivity measurement with continuous wave laser illumination. **b**, Conductivity as a function of photo-excited carrier density showing an insulator to metal transition.

between leads. The measured conductivity at zero gate voltage is purely from the photo-excited electron hole system, as the low temperature and low defect density totally suppress other kinds of doping. Figure 5.1b shows conductivity as a function of photo-excited carrier density. The abrupt rise of photoconductivity by more than two orders of magnitude in the range of 10^{12} to 10^{14} cm^{-2} carrier density characterizes an insulator to metal transition[108]. While at low densities, the electrons and holes are tightly bound into single neutral quasiparticles resistant to external DC electric field, at high densities, the Coulomb interactions are effectively screened leading to adjacent sheets of conducting electrons and holes, flowing in opposite directions under DC electric field.

Compared to optical probes involving transition from/to the ground state, the electrical[108] and optical[109,110] (THz) conductivity probes all electron hole species at arbitrarily large ***k***. The Mott transition shown here was realized in an optically dark heterobilayer, owing to charge separation and large momentum mismatch between electrons and holes[39]. The carrier density used here was calibrated from optically bright heterobilayers at similar conditions. The gate

doping of up to 3×10^{12} cm^{-2} carriers into the system does not remarkably change the conductivity even at the lowest optical doping density, confirming that the heterobilayer was much more doped from optical excitations.

5.2 Time-resolved diffusion

The other phenomena we use to characterize this metal insulator transition is diffusion. The conduction and diffusion are two sides of the same coin, both directly related to the momentum relaxation time during transport processes. To measure diffusion, we excite at a certain spot of the heterobilayer and observe the spatial expansion of the electron hole system by scanning confocal microscopy. During the transport process, tiny amount of electrons and holes can directly recombine across the interface and emit photoluminescence (PL) around 1.3 eV, which was used as a sensitive probe of the diffusion[47,49,111].

We first inject electrons and holes of known amount into a diffraction-limited spot by an ultrafast pulse (~100 fs) and resolve the PL intensity in time and space. The diffusion-reaction equation with a first order decay term has an analytical solution of expanding Gaussian distribution where the spatial variance, σ^2, scales linearly with time with a slope proportional to the diffusion coefficient. The radial profile of PL at each time delay was fit to Gaussian functions. The spatial variance as a function of time (Figure 5.2b) deviates from linear relationship because of different diffusion coefficients from different species. We extracted this time-dependent effective diffusion coefficient, $D(t) = \frac{\mathrm{d}\sigma^2(t)}{\mathrm{d}t}$, from the slope of the curve (Figure 5.2e). The two clear transitions in the $D(t)$ curves in the $t < 10^1$ ns and $t > 10^2$ ns range is assigned to the Mott transition and moiré exciton trapping, as explained below.

Within time resolution, a rapid expansion happens especially at high excitation densities. As a result, the observed initial spatial variance increases with excitation density (Figure 5.2f).

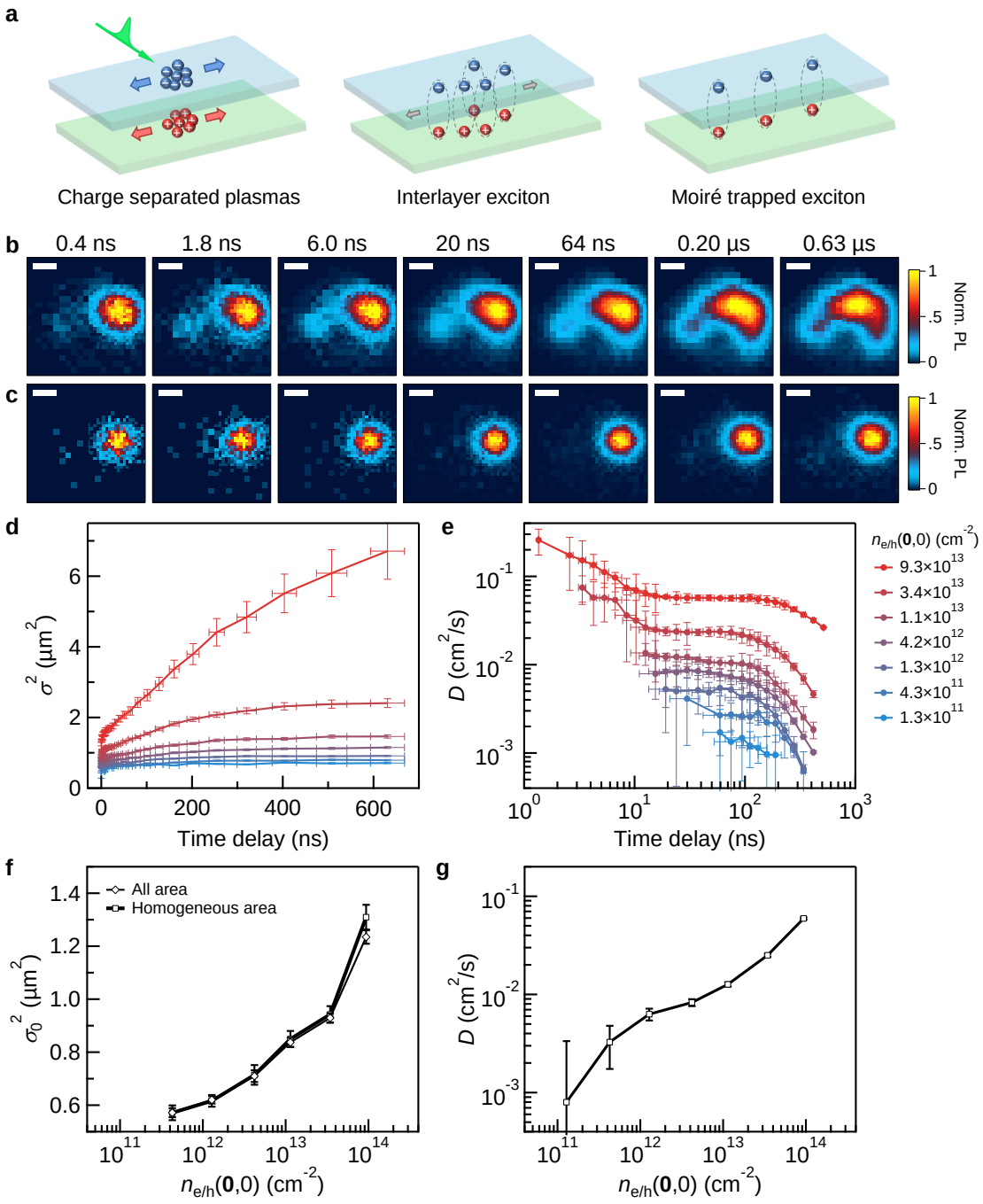

Figure 5.2 | Time-resolved diffusion in $MoSe_2/WSe_2$ heterobilayer. a, Schematics showing transition between electron hole plasmas, interlayer excitons and moiré trapped excitons. **b** and **c**, Photoluminescence image at different time delay at high (9.3×10^{13} cm^{-2}, **b**) and low (1.3×10^{12} cm^{-2}, c) excitations densities. Scale bar, 2 µm. **d** and **e**, Spatial variance σ^2 (**d**) and effective diffusion coefficient (**e**) as a function of time at different excitation densities. **f** and **g**, The observed initial spatial variance (**f**) and plateau diffusion coefficient (**g**) as a function of initial excitation density.

Taking the initial spatial profile of PL at low excitation as an upper limit of excitation profile ($\sigma_0^2 < 0.6\ \mu m^2$) and the time resolution as an upper limit of expansion time ($\Delta t < 0.25$ ns), the initial diffusion coefficient at highest excitation density (~10^{14} cm^{-2}) is estimated to be at least 15 cm^2/s. This rapid expansion is a combined effect of ballistic transport character and dipolar repulsive drift as reported in coupled quantum wells[112] as well as screened Coulomb scattering at high carrier densities. It explains the low Auger recombination rate at seemingly high excitation densities[103]. The carrier density was substantially reduced from excitation density during the rapid expansion from diffraction-limited spot ($\sigma_0^2 \approx 0.05\ \mu m^2$), leading to the Mott transition. The tail of this Mott transition was observed in the drop of effective diffusion coefficient in the t < 10^1 ns range. After ~ 20 ns, the whole electron hole system is below Mott density and the transport behavior becomes purely diffusive: the spatial variance starts to scale linearly with time and the effective diffusion coefficient reaches a plateau. This atomically separated interlayer exciton shows smaller diffusion coefficients than traditional coupled quantum wells, consistent with the decreasing diffusion coefficient with decreasing barrier width observed therein[112]. The interlayer exciton is still subject to moiré potential formed by spatially varying interlayer distance and can be further confined to local moiré traps, accompanied by loss of kinetic energy and screening of dipolar repulsion. Therefore, the plateau interlayer exciton diffusion coefficient varies by two orders of magnitude depending on exciton density (Figure 5.2g) and the effective diffusion coefficient drops again in the $t > 10^2$ ns range when higher density excitons decay and get trapped (Figure 5.2e).

5.3 Steady-state diffusion

We also excited the heterobilayer at a fixed spot by continuous wave (CW) laser and map the PL spectra. In this case, the generation, recombination and diffusion of interlayer electron

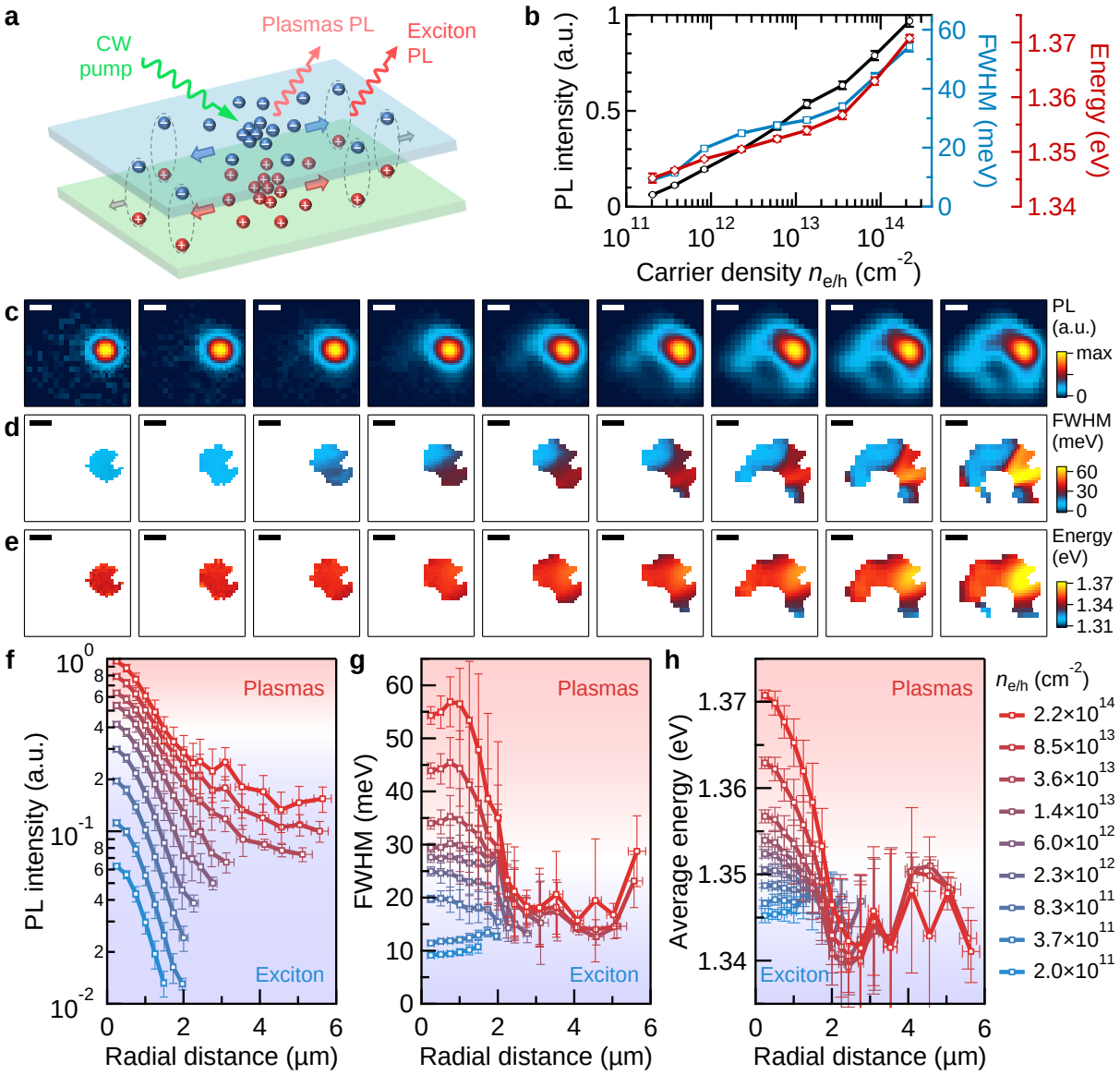

Figure 5.3 | Steady-state diffusion in $MoSe_2/WSe_2$ heterobilayer. a, Schematics showing spatial phase separation in steady-state diffusion experiment. **b**, PL intensity, FWHM and average energy as a function of carrier density at excitation spot. **c**, **d** and **e**, image of PL intensity (**c**), FWHM (**d**) and average energy (**e**) at different excitation densities, from 2.0×10^{11} cm^{-2} (leftmost) to 2.2×10^{14} cm^{-2} (rightmost), as listed in the legend of h. Scale bar, 2 μm. **f**, **g** and **h**, PL intensity (**f**), FWHM (**g**) and average energy (**h**) as a function of radial distance from excitation spot at different excitation densities. The plasmas phase can be seen at high excitation densities within ~ 2 μm of the excitation spot.

hole system reach a steady state everywhere in the heterobilayer. While the center spot has been shown to reach high carrier densities up to 10^{14} cm^{-2}, the carrier density at long enough radial distance has to converge to zero with finite injection. The spatial distribution of carrier density naturally contrast between different phases and can be probed by PL spectrum[113]. Therefore a Mott transition could be directly imaged in real space. Figure 5.3b shows the PL characteristics at the excitation spot as a function of local carrier density. A large broadening of PL spectrum signals the giant renormalization of continuum states to below the excitonic resonance and the conversion from well-defined interlayer exciton to correlated electron hole plasma; the PL average energy also blue shifts with increasing carrier density as a result of dipolar repulsion. At high excitation densities, the spatial map of PL FWHM (Figure 5.3d) and average energy (Figure 5.3e) shows clear phase separation where the electron hole plasma phase resides within ~ 2 μm from the spot of continuous pumping surrounded by the interlayer exciton phase with value similar to low excitation density cases. As a comparison, at low excitation densities, the PL linewidth is rather homogenous over the whole diffusion length indicating the existence of a single interlayer exciton phase. At our highest excitation densities, the FWHM could increase by ~ 45 meV and the average energy by ~ 25 meV (Fig. 5.3g and h).

5.4 Conclusion

In conclusion, the Mott transition in the photo-excited electron hole system in semiconducting heterobilayers is confirmed by both conduction and diffusion experiments and directly observed in real time and space. At high excitation densities, the system consists of two atomically close layer of plasmas of opposite charges. Under effectively screened Coulomb correlation, the electrons and holes move relatively independently in adjacent layers, yielding the metallic conductivity. In contrast, at low excitation densities, the electrons and holes are bound

into neutral interlayer excitons with finite diffusion coefficient and negligible conductivity. Furthermore, the interlayer excitons can be trapped in moiré potential at extremely low density and temperature, consistent with their quantum dot like photoluminescence spectra[40]. Previous reports demonstrated the emergence of superconductivity in ionic liquid gated monolayer TMDCs at around 10^{14} cm^{-2} and 10 K[114]. The lack of quantum behavior in current study is likely a result of high temperature of the interlayer electron hole system and may be overcome by increasing its lifetime through BN intercalation[51,53].

This page intentionally left blank

Chapter 6

The Nature of Trion in Monolayer $MoSe_2$

In 2D semiconductors, the photo-excited electrons and holes can be Coulomb bound to form not only excitons, a two-body species, but also three-body species, known as charged excitons or trions which can be negative or positive depending on its composition. The existence of trion pushed the analogy between exciton and hydrogen further to the analogy between trion and dihydrogen cation (H_2^+) or hydrogen anion (H^-), indicating that the chemistry of hydrogen species can be reproduced in photo-excited semiconductors[9]. Beyond this fundamental importance, the trion is of interest to realistic applications of excitonic materials because of its ease of electrical manipulation as a carrier of both energy and charge[115].

In 2D TMDCs, the trion is first discovered in 2013 in MoS_2[14] and $MoSe_2$[15] monolayers. The trion binding energy is about (20~30) meV, two to three orders of magnitude larger than in 3D materials[116] and an order of magnitude larger than conventional 2D quantum well systems[21]. Despite the numerous electric and magnetic field dependence studies that supports its existence, the nature of trion in 2D TMDCs is still under debate. MacDonald and coworkers pointed out that the correct picture at finite doping should instead be exciton interacting with a Fermi sea of charge carriers forming attractive and repulsive exciton polarons[22,23]; Dery and coworkers proposed a different mechanism of photoluminescence in which the trion is only a virtual species formed when a localized charge captures an exciton by emitting an optical phonon and the alleged trion binding energy is actually the optical phonon energy[24].

In this chapter, I will present our answer to the nature of trion in monolayer $MoSe_2$. Section 1.1 shows the surprising disorder tolerance of trion binding energy which allows a

precise measurement of it through photoluminescence imaging. In section 1.2 and 1.3 the Mott transition was explored in monolayer $MoSe_2$ by photoluminescence spectroscopy and imaging techniques. Section 1.4 concludes that the trion in monolayer $MoSe_2$ is a robust and mobile species.

6.1 Disorder tolerant trion binding energy

The photoluminescence spectra of monolayer $MoSe_2$ features two peaks that was assigned to the exciton and trion. It was shown that by BN encapsulation the linewidth can be reduced to 2 meV, close to its 1 meV intrinsic limit[12]. Therefore in BN encapsulated monolayer $MoSe_2$, the assigned exciton and trion peaks are well-separated, making it ideal system to study and compare two-body and three-body states. The difference in energy between those two peaks is attributed to the trion binding energy, as can be deduced from the chemical equations of photoluminescence:

$$\mathrm{X} \rightarrow \hbar\omega_{\mathrm{X}}$$
$$\mathrm{X}^{-} \rightarrow \hbar\omega_{\mathrm{X}^{-}} + \mathrm{e}^{-}$$

where $\hbar\omega_{\mathrm{X}}$ and $\hbar\omega_{\mathrm{X}^{-}}$ are the energies of emission for exciton and trion. The formation of trion

$$\mathrm{X} + \mathrm{e}^{-} \rightarrow \mathrm{X}^{-} + \hbar\left(\omega_{\mathrm{X}} - \omega_{\mathrm{X}^{-}}\right)$$

accompanies the release of energy $E_{\mathrm{B}}^{\mathrm{X}^{-}} = \hbar\left(\omega_{\mathrm{X}} - \omega_{\mathrm{X}^{-}}\right)$. In doped semiconductors, the energy difference includes not only trion binding energy but an additional term of Fermi energy of electrons[14].

We obtained image of BN encapsulated monolayer $MoSe_2$ by scanning confocal microscopy where in every spot a PL spectrum is measured (Figure 6.1a and b). Here the spots

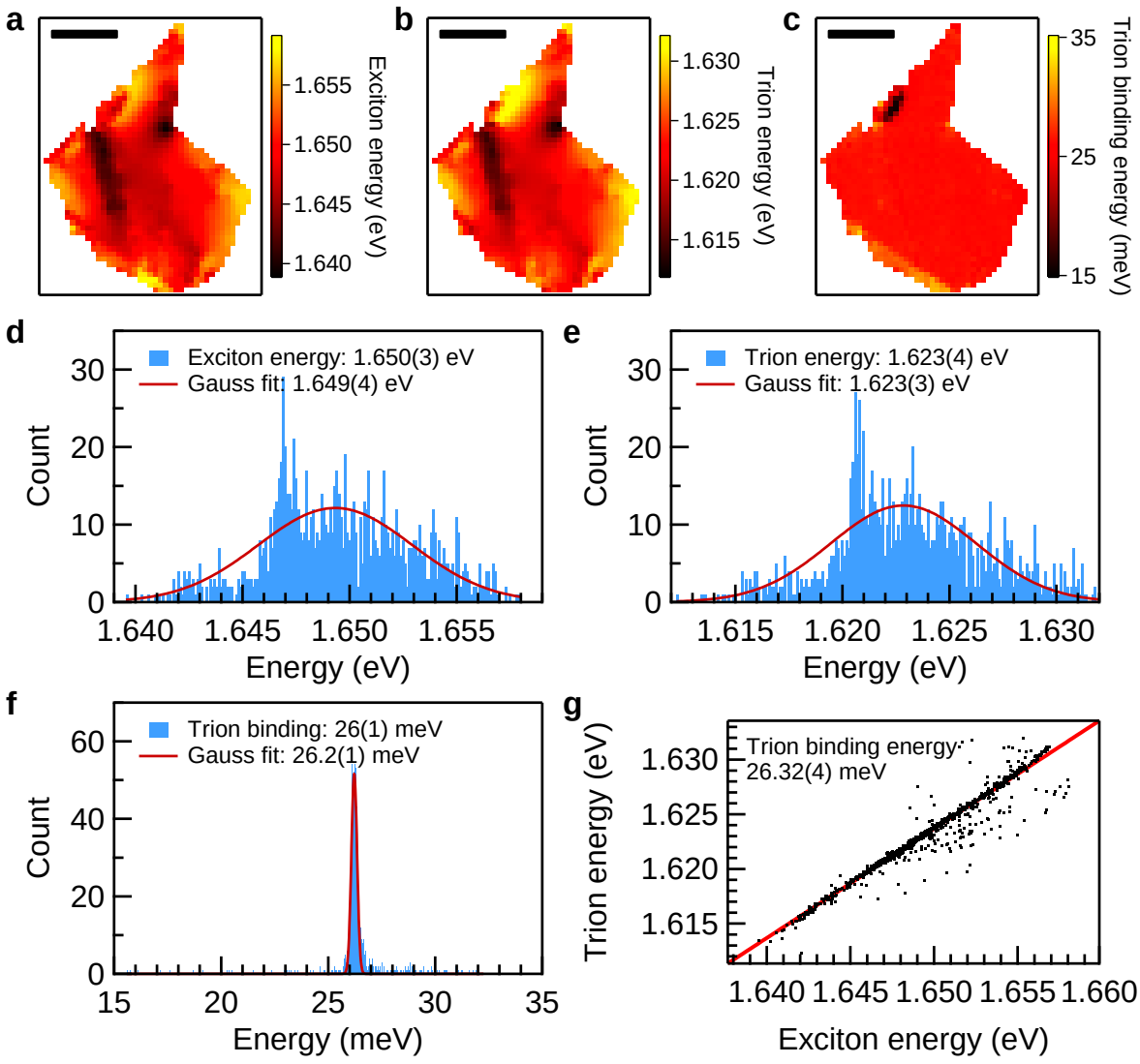

Figure 6.1 | Disorder tolerant trion binding energy in monolayer $MoSe_2$. a, b and **c**, image of exciton energy (**a**), trion energy (**b**) and trion binding energy (**c**) of the MoSe2 sample. Scale bar, 5 μm. **d**, **e** and **f**, Histogram of exciton energy (**d**), trion energy (**e**) and trion binding energy (**f**) from top to bottom. **g**, Trion energy plotted against exciton energy. Each black dot corresponds to a diffraction limited spot in the image. The red line is a linear fit with unity slope.

are spaced 0.25 μm apart, a distance roughly equal to the resolution limit of optical imaging. Each spot therefore represents independent local energy levels of a 6×10^{-10} cm^2 $MoSe_2$ sample. The average energy of exciton and trion peaks are extracted by weighting over PL intensity. The

energies are then binned to histograms. Both exciton and trion peaks fluctuate in ~ 20 meV range with a standard deviation of about 3.5 meV.

Surprisingly, the fluctuation of trion binding energy is more an order of magnitude smaller than that of the exciton and trion energy levels. In other words, the exciton and trion are "locked" in energy difference and fluctuate as a whole around the energy landscape of the sample. This effect can be examined is two approaches. The trion binding energy can be imaged (Figure 6.1c) and histogrammed (Figure 6.1d) to show the range of fluctuation of about 1 meV and the standard deviation of about 1.2 meV. On the other hand, the trion energy can be plotted against exciton energy for each spot (Figure 6.1e). The scattered points accumulate along a straight line with unity slope. A linear fitting with unity slope gives a trion binding energy of 26.29±0.04 meV.

The disorder response of band gap and exciton binding energy in monolayer WS_2, measured by reflectance imaging, has been reported to be tens of meV[117]. In contrast to traditional source of disorder like local fluctuations of chemical and structural composition, doping or strain, the disorder in 2D monolayers is based entirely on the fluctuation of external dielectric environment[117]. In our sample, the exciton and trion energies do vary in the similar range, however the trion binding energy is exceptionally tolerant to the dielectric disorder.

The precise determination of this trion binding energy makes it possible to test the nature of trion. Temperature dependence of trion binding energy and optical phonon energy is performed to investigate their correlations (Figure 6.2). The temperature was varied from 4 K to 60 K above which the trion is thermally dissociated. The energy distributions of exciton, trion and trion binding energy at elevated temperatures are similar to the 4K case while the whole distribution is shifting in a consistent direction (Figure 6.2a-c). In this temperature range the

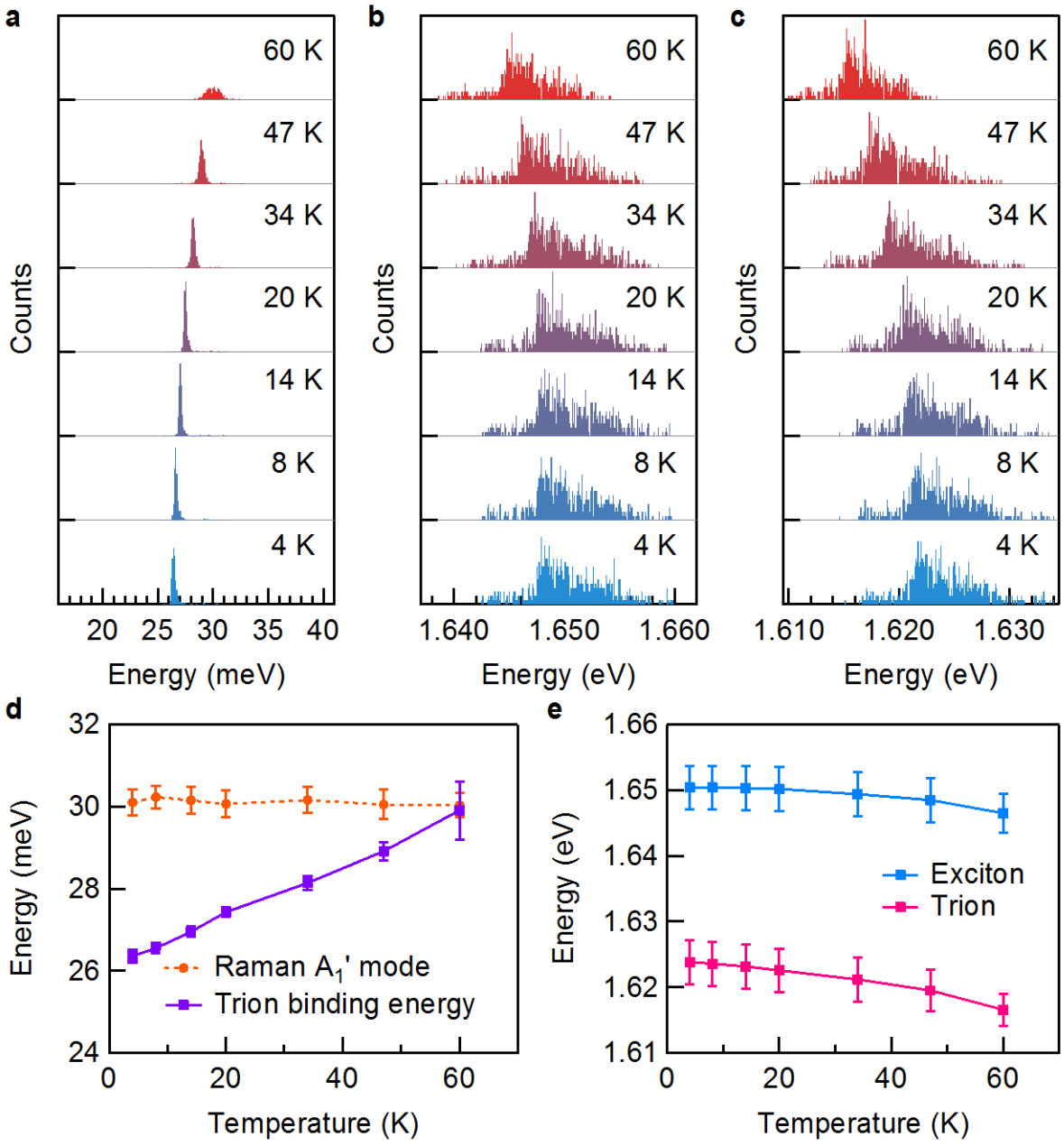

Figure 6.2 | Temperature dependence of trion binding energy in monolayer $MoSe_2$. a, b and **c**, Temperature dependent histogram of trion binding energy (**a**), exciton energy (**b**) and trion energy (**c**). **d**, Trion binding energy as a function of temperature. **e**, Exciton and trion energy as a function of temperature.

energies of exciton and trion both shift to lower values by several meV (Figure 6.2e), consistent with the traditional temperature dependence of semiconductor band gap[118] and similar previous

reports on $MoSe_2$[15]. The trion binding energy blue-shifts by 3 meV (Figure 6.2d). In contrast, the energy of the Raman A_1' peak, also precisely determined, is nearly constant over this temperature range and at a different value (33 meV) from the trion binding energy. The disagreement of temperature dependence between trion binding energy and optical phonon energy thus disfavors the virtual phonon theory where the trion is a virtual species and the energy released during virtual trion formation is attributed to optical phonon emission[24].

6.2 Robust trionic emission across Mott transition

The Mott transition of monolayer TMDCs has been demonstrated by transient reflectance spectroscopy. The upper limit of Mott density, estimated by the empirical formula, $n_{Mott} \approx \left(\pi a_B^2\right)^{-1}$, is about 3×10^{13} cm^{-2} for the exciton Bohr radius $a_B \approx 1$ nm in monolayers. The time-resolved reflectance contrast (proportional to absorption) clearly shows a total bleaching of exciton peaks, the renormalization of band gap to lower than exciton energy and the stimulated emission near the renormalized band gap. Here we record time-resolved photoluminescence (TRPL) by time-correlated single photon counting (TCSPC) technique to study the emission of monolayer $MoSe_2$ across Mott transition.

The PL at lower excitation density (1×10^{12} cm^{-2}) show two well-separated peaks just like the PL obtained by continuous wave (CW) excitation (Figure 6.3a). The absolute intensity of trion peak is higher than the exciton one due to the above band gap excitation and impact ionization mechanism of trion formation. At excitation density higher than the Mott density (4×10^{13} cm^{-2}), both the exciton and trion emission are weaken, with additional spectrally flat emission at other energies, consistent with the bleaching and broad absorption observed in time resolved absorption experiments (Figure 6.3b). While the emission at excitonic resonances above Mott transition is theoretically well-known to be from the Coulomb enhancement of cross

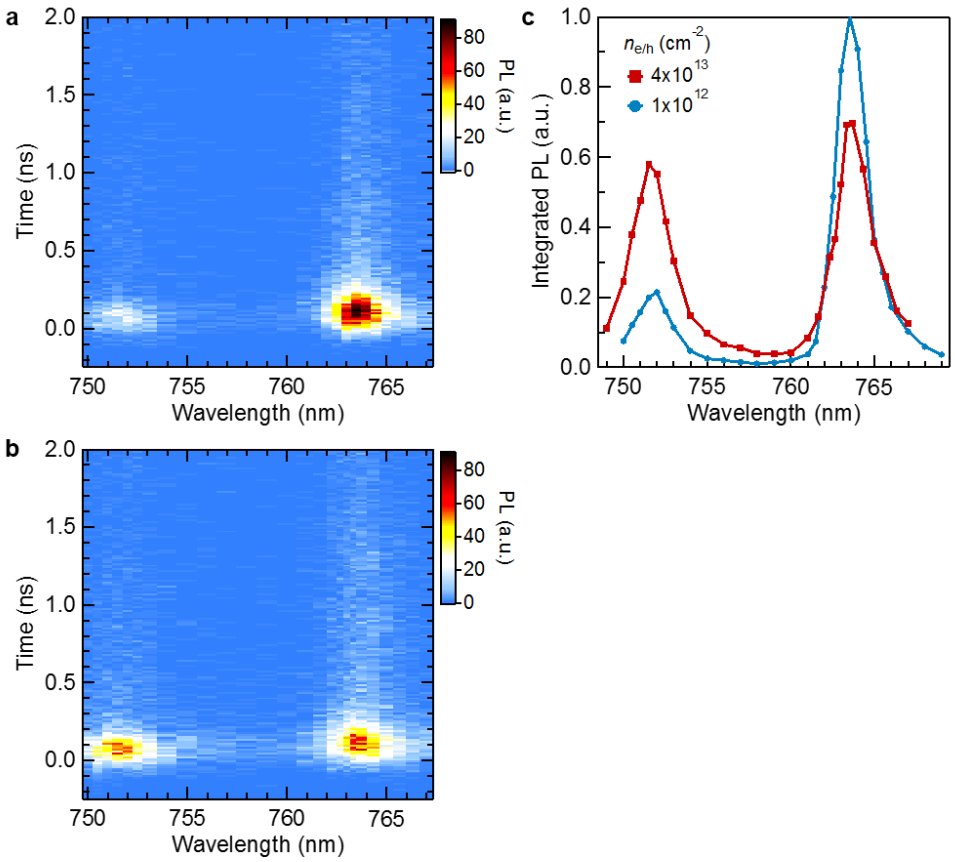

Figure 6.3 | Time and energy resolved photoluminescence of monolayer $MoSe_2$. a and **b**, time and wavelength dependent photoluminescence of monolayer $MoSe_2$ at initial excitation densities of 1×10^{12} cm^{-2} (**a**) and 4×10^{13} cm^{-2} (**b**). **c**, PL spectra integrated for $r < 1$ μm and -0.1 ns < t < 0.2 ns at two excitation densities.

section at those energies[119], the similar trionic enhancement was not reported before. Similar to the excitonic resonance, the trionic resonance energy is also robust against increased screening at elevated carrier densities. This means that in the electron-hole plasma, the transient correlation can also form between three particles and emit near the trionic resonance. The three-body correlation should be harder than the two-body correlation, therefore the cross section of trionic emission should decrease relatively to the excitonic emission (Figure 6.3c). At higher excitation density and early time, we do see an increase of excitonic to trionic emission intensity ratio; this ratio then decreases over time following the carrier density decay (Figure 6.3b).

6.3 Diffusion of exciton, trion and electron hole plasma

With the knowledge of spectral change over Mott transition, the diffusion of exciton, trion and the electron hole plasma in monolayer $MoSe_2$ is measured by time and energy resolved PL imaging with a fixed ultrafast excitation at a diffraction limit spot.

We first integrate the intensity of excitonic and trionic emissions in corresponding energy range. At lower excitation densities, a faster diffusion of trion than exciton is clearly seen (Figure 6.4 a and b). The solution of diffusion equation with a first order decay term is a 2D Gaussian distribution with spatial variance linearly increasing in time. The slope of such linear relations is twice the diffusion constant. The diffusion and decay of exciton and trion in monolayer TMDCs is within the time resolution of TCSPC thus not resolvable by this technique. However, the diffusion constant can still be estimated by $\sigma^2 = 2Dt + \sigma_0^2$ where t is taken to be the time resolution of TCSPC and σ_0 is inferred from diffraction limit. The estimated diffusion constants of exciton and trion are about 26 cm^2/s and 76 cm^2/s respectively, comparable to literature value in quantum well systems[115]. Since the trion has higher effective mass than exciton which even reportedly induce negative photoconductivity in monolayer MoS_2, the faster apparent diffusion has to be attributed to the drift motion from repulsive potential among them because trion is a charged species. This observation evinces that the trion in monolayer $MoSe_2$ is an individual mobile charge carrier instead of an exciton traveling in Fermi sea of electrons.

At excitation densities about Mott density, the electron hole plasma should diffuse as a single species with free carrier diffusion characteristics. Since the carrier density is changing in time and space, the spectral weight between excitonic and trionic emissions will also change accordingly. Near the excitation spot and at early times, the absolute intensity of trionic emission will be weaker than that at farther away spot and later times giving rise to the formation of a ring

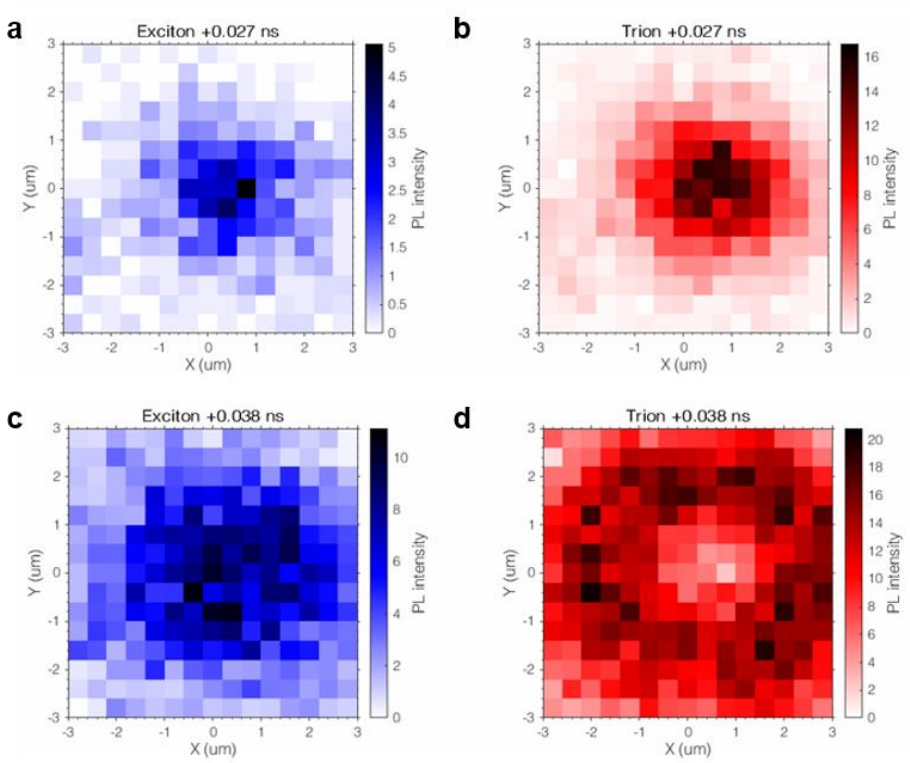

Figure 6.4 | Time-resolved diffusion of exciton, trion and plasma in $MoSe_2$. a and **b**, early-time photoluminescence image integrated at exciton (**a**) and trion (**b**) energy ranges for 1×10^{12} cm^{-2} excitation density. **c** and **d**, early-time photoluminescence image integrated at excitonic resonance (**a**) and trionic resonance (**b**) energy ranges for 4×10^{13} cm^{-2} excitation density.

pattern; the excitonic emission is positively correlated with carrier densities therefore the diffusion still yields a near Gaussian distribution (Figure 6.4 c and d). The plasma diffusion constant, estimated from same method stated above, is about 610 cm^2/s. After the unresolvable fast initial expansion, the whole system is below Mott density and the diffusion rate is similar to the low density case.

The ring pattern formation in conventional quantum wells systems has been under intense debate for two decades. While some assign the ring to exciton condensation[120], others point out that the ring could be formed by Mott transition and kinetic interplay between exciton and electron hole plasma[113]. In this work, we take advantage of the two robust emission features with

density dependent ratio in monolayer $MoSe_2$ to prove that the formation of ring could be due to the Mott transition. After all, trion as a fermion cannot form Bose-Einstein condensate even though its diffusion pattern at high densities is a ring. This results also impose questions on the previously reported diffusional ring formation in WS_2 at room temperature where the peak was broad and not resolved and the ring was attributed to Auger recombination or heat effect[121].

The energy resolution can be exploited to track energy shift during diffusion due to local disorder. As previously discussed, the local energy of trion fluctuates by ~ 20 meV in the whole sample. In the spatial range where we measured diffusion, this range is about 10 meV. The time and energy resolved diffusion process actually show the shifting of trionic emission energy during diffusion and the energies are similar to local trion energy. In other words, the non-equilibrium carrier density distribution drives the plasma along the fluctuating energy landscape on the $MoSe_2$ sample.

6.4 Conclusion

In conclusion, the novel observations on monolayer $MoSe_2$ enabled by high quality crystals and time and energy resolved photoluminescence imaging help resolve the nature of trion therein. The precisely measured disorder tolerant trion binding energy contradicts optical phonon in temperature dependence, disfavoring the virtual trion theory. The higher diffusion constant of trion than exciton proves that it is a mobile species carrying charge, in contradiction to the exciton polaron theory. Above Mott transition, the trionic emission is weaken but still exist as a dominating emission channel. The ring pattern forms only at trionic emission energies for above Mott excitation densities and can be explained by diffusion induced Mott transition in real time and space. We conclude that the trion in monolayer $MoSe_2$ is a robust and mobile carrier of charge and energy.

References

1. Mak, K. F., Lee, C., Hone, J., Shan, J. & Heinz, T. F. Atomically thin MoS_2: a new direct-gap semiconductor. *Phys. Rev. Lett.* **105**, 136805 (2010).
2. Wang, G. *et al.* Colloquium: excitons in atomically thin transition metal dichalcogenides. *Rev. Mod. Phys.* **90**, 021001 (2018).
3. Liu, G. Bin, Xiao, D., Yao, Y., Xu, X. & Yao, W. Electronic structures and theoretical modelling of two-dimensional group-VIB transition metal dichalcogenides. *Chem. Soc. Rev.* **44**, 2643 (2015).
4. Cappelluti, E., Roldán, R., Silva-Guillén, J. A., Ordejón, P. & Guinea, F. Tight-binding model and direct-gap/indirect-gap transition in single-layer and multilayer MoS_2. *Phys. Rev. B* **88**, 075409 (2013).
5. Xiao, D., Liu, G. Bin, Feng, W., Xu, X. & Yao, W. Coupled spin and valley physics in monolayers of MoS_2 and other group-VI dichalcogenides. *Phys. Rev. Lett.* **108**, 196802 (2012).
6. Yao, W., Xiao, D. & Niu, Q. Valley-dependent optoelectronics from inversion symmetry breaking. *Phys. Rev. B* **77**, 235406 (2008).
7. Liu, G. Bin, Shan, W. Y., Yao, Y., Yao, W. & Xiao, D. Three-band tight-binding model for monolayers of group-VIB transition metal dichalcogenides. *Phys. Rev. B* **88**, 085433 (2013).
8. Kormányos, A; Burkard, G.; Gmitra, M.; Fabian, J; Zólyomi, V.; Drummond, ND; Fal'ko, V. *et al.* k·p theory for two-dimensional transition metal dichalcogenide semiconductors. *2D Mater.* **2**, 22001 (2015).

9. Klingshirn, C. *Semiconductor Optics*. (Springer, 2007).

10. Chernikov, A. *et al.* Exciton binding energy and nonhydrogenic Rydberg series in monolayer WS_2. *Phys. Rev. Lett.* **113**, 076802 (2014).

11. Haug, H. & Koch, S. W. *Quantum theory of the optical and electronic properties of semiconductors*. (World Scientific, 2009).

12. Ajayi, O. A. *et al.* Approaching the intrinsic photoluminescence linewidth in transition metal dichalcogenide monolayers. *2D Mater.* **4**, 031011 (2017).

13. Edelberg, D. *et al.* Approaching the intrinsic limit in transition metal diselenides via point defect control. *Nano Lett.* **19**, 4371 (2019).

14. Mak, K. F. *et al.* Tightly bound trions in monolayer MoS_2. *Nat. Mater.* **12**, 207 (2013).

15. Ross, J. S. *et al.* Electrical control of neutral and charged excitons in a monolayer semiconductor. *Nat. Commun.* **4**, 1474 (2013).

16. You, Y. *et al.* Observation of biexcitons in monolayer WSe_2. *Nat. Phys.* **11**, 477 (2015).

17. Barbone, M. *et al.* Charge-tuneable biexciton complexes in monolayer WSe_2. *Nat. Commun.* **9**, 3721 (2018).

18. Ye, Z. *et al.* Efficient generation of neutral and charged biexcitons in encapsulated WSe_2 monolayers. *Nat. Commun.* **9**, 3718 (2018).

19. Chen, S.-Y. Y., Goldstein, T., Taniguchi, T., Watanabe, K. & Yan, J. Coulomb-bound four- and five-particle intervalley states in an atomically-thin semiconductor. *Nat. Commun.* **9**, 3717 (2018).

20. Li, Z. *et al.* Revealing the biexciton and trion-exciton complexes in BN encapsulated WSe_2. *Nat. Commun.* **9**, 3719 (2018).

21. Kheng, K. *et al.* Observation of negatively charged excitons X^- in semiconductor quantum

wells. *Phys. Rev. Lett.* **71**, 1752 (1993).

22. Efimkin, D. K. & MacDonald, A. H. Many-body theory of trion absorption features in two-dimensional semiconductors. *Phys. Rev. B* **95**, 035417 (2017).
23. Sidler, M. *et al.* Fermi polaron-polaritons in charge-tunable atomically thin semiconductors. *Nat. Phys.* **13**, 255 (2017).
24. Van Tuan, D., Jones, A. M., Yang, M., Xu, X. & Dery, H. Virtual trions in the photoluminescence of monolayer transition-metal dichalcogenides. *Phys. Rev. Lett.* **122**, 217401 (2019).
25. Mott, N. F. Metal-insulator transition. *Rev. Mod. Phys.* **40**, 677 (1968).
26. Guerci, D., Capone, M. & Fabrizio, M. Exciton Mott transition revisited. *Phys. Rev. Mater.* **3**, 054605 (2019).
27. Zimmermann, R. Nonlinear optics and the Mott transition in semiconductors. *Phys. status solidi* **146**, 371 (1988).
28. Tränkle, G. *et al.* General relation between band-gap renormalization and carrier density in two-dimensional electron-hole plasmas. *Phys. Rev. B* **36**, 6712 (1987).
29. Chernikov, A., Ruppert, C., Hill, H. M., Rigosi, A. F. & Heinz, T. F. Population inversion and giant bandgap renormalization in atomically thin WS_2 layers. *Nat. Photonics* **9**, 466 (2015).
30. Mak, K. F. *et al.* Measurement of the optical conductivity of graphene. *Phys. Rev. Lett.* **101**, 196405 (2008).
31. Cunningham, P. D., Hanbicki, A. T., McCreary, K. M. & Jonker, B. T. Photoinduced bandgap renormalization and exciton binding energy reduction in WS_2. *ACS Nano* **11**, 12601 (2017).

32. Liu, F., Ziffer, M. E., Hansen, K. R., Wang, J. & Zhu, X. Direct determination of band-gap renormalization in the photoexcited monolayer MoS_2. *Phys. Rev. Lett.* **122**, 246803 (2019).

33. Geim, A. K. & Grigorieva, I. V. Van der Waals heterostructures. *Nature* **499**, 419 (2013).

34. Cao, Y. *et al.* Unconventional superconductivity in magic-angle graphene superlattices. *Nature* **556**, 43 (2018).

35. Cao, Y. *et al.* Correlated insulator behaviour at half-filling in magic-angle graphene superlattices. *Nature* **556**, 80 (2018).

36. Hong, X. *et al.* Ultrafast charge transfer in atomically thin MoS_2/WS_2 heterostructures. *Nat. Nanotechnol.* **9**, 682 (2014).

37. Ma, E. Y. *et al.* Recording interfacial currents on the subnanometer length and femtosecond time scale by terahertz emission. *Sci. Adv.* **5**, eaau0073 (2019).

38. Jin, C. *et al.* Ultrafast dynamics in van der Waals heterostructures. *Nat. Nanotechnol.* **13**, 994 (2018).

39. Yu, H., Wang, Y., Tong, Q., Xu, X. & Yao, W. Anomalous light cones and valley optical selection rules of interlayer excitons in twisted heterobilayers. *Phys. Rev. Lett.* **115**, 187002 (2015).

40. Seyler, K. L. *et al.* Signatures of moiré-trapped valley excitons in $MoSe_2/WSe_2$ heterobilayers. *Nature* **567**, 66 (2019).

41. Yu, H., Liu, G.-B., Tang, J., Xu, X. & Yao, W. Moiré excitons: From programmable quantum emitter arrays to spin-orbit-coupled artificial lattices. *Sci. Adv.* **3**, e1701696 (2017).

42. Rivera, P. *et al.* Observation of long-lived interlayer excitons in monolayer $MoSe_2$-WSe_2

heterostructures. *Nat. Commun.* **6**, 6242 (2015).

43. Ross, J. S. *et al.* Interlayer exciton optoelectronics in a 2D heterostructure p-n junction. *Nano Lett.* **17**, 638 (2017).

44. Gillen, R. & Maultzsch, J. Interlayer excitons in $MoSe_2/WSe_2$ heterostructures from first principles. *Phys. Rev. B* **97**, 165306 (2018).

45. Kunstmann, J. *et al.* Momentum-space indirect interlayer excitons in transition-metal dichalcogenide van der Waals heterostructures. *Nat. Phys.* **14**, 801 (2018).

46. Unuchek, D. *et al.* Room-temperature electrical control of exciton flux in a van der Waals heterostructure. *Nature* **560**, 340 (2018).

47. Jauregui, L. A. *et al.* Electrical control of interlayer exciton dynamics in atomically thin heterostructures. *Science* **366**, 870 (2019).

48. Paik, E. Y. *et al.* Interlayer exciton laser of extended spatial coherence in atomically thin heterostructures. *Nature* **576**, 80 (2019).

49. Rivera, P. *et al.* Valley-polarized exciton dynamics in a 2D semiconductor heterostructure. *Science* **351**, 688 (2016).

50. Kim, J. *et al.* Observation of ultralong valley lifetime in WSe_2/MoS_2 heterostructures. *Sci. Adv.* **3**, e1700518 (2017).

51. Fogler, M. M., Butov, L. V. & Novoselov, K. S. High-temperature superfluidity with indirect excitons in van der Waals heterostructures. *Nat. Commun.* **5**, 4555 (2014).

52. Wu, F. C., Xue, F. & Macdonald, A. H. Theory of two-dimensional spatially indirect equilibrium exciton condensates. *Phys. Rev. B* **92**, 165121 (2015).

53. Wang, Z. *et al.* Evidence of high-temperature exciton condensation in two-dimensional atomic double layers. *Nature* **574**, 76–80 (2019).

54. Boyd, R. W. *Nonlinear optics*. (Academic Press, 2003).

55. Fox, M. *Optical properties of solids*. (Oxford University Press, 2010).

56. Kuzmenko, A. B. Kramers-Kronig constrained variational analysis of optical spectra. *Rev. Sci. Instrum.* **76**, 083108 (2005).

57. Li, Y. *et al.* Measurement of the optical dielectric function of monolayer transition-metal dichalcogenides: MoS_2, $MoSe_2$, WS_2, and WSe_2. *Phys. Rev. B* **90**, 205422 (2014).

58. Li, Y. *et al.* Probing symmetry properties of few-layer MoS_2 and h-BN by optical second-harmonic generation. *Nano Lett.* **13**, 3329 (2013).

59. Mannebach, E. M. *et al.* Ultrafast electronic and structural response of monolayer MoS_2 under intense photoexcitation conditions. *ACS Nano* **8**, 10734 (2014).

60. Schaibley, J. R. *et al.* Directional interlayer spin-valley transfer in two-dimensional heterostructures. *Nat. Commun.* **7**, 13747 (2016).

61. Wang, G. *et al.* Giant enhancement of the optical second-harmonic emission of WSe_2 monolayers by laser excitation at exciton resonances. *Phys. Rev. Lett.* **114**, 097403 (2015).

62. Klein, J. *et al.* Electric-field switchable second-harmonic generation in bilayer MoS_2 by inversion symmetry breaking. *Nano Lett.* **17**, 392 (2017).

63. Becker, W. *The bh TCSPC Handbook*. (Becker & Hickl GmbH, 2014).

64. *Model SR830 DSP Lock-In Amplifier*. (Stanford Research Systems, 2011).

65. Zhu, X. *et al.* Charge transfer excitons at van der Waals interfaces. *J. Am. Chem. Soc.* **137**, 8313 (2015).

66. Wilson, N. R. *et al.* Determination of band offsets, hybridization, and exciton binding in 2D semiconductor heterostructures. *Sci. Adv.* **3**, e1601832 (2017).

67. Chiu, M.-H. *et al.* Determination of band alignment in the single-layer MoS_2/WSe_2

heterojunction. *Nat. Commun.* **6**, 7666 (2015).

68. Dean, C. R. *et al.* Boron nitride substrates for high-quality graphene electronics. *Nat. Nanotechnol.* **5**, 722 (2010).

69. Cui, X. *et al.* Multi-terminal transport measurements of MoS_2 using a van der Waals heterostructure device platform. *Nat. Nanotechnol.* **10**, 534 (2015).

70. Wang, L. *et al.* One-dimensional electrical contact to a two-dimensional material. *Science* **342**, 614 (2013).

71. Cheiwchanchamnangij, T. & Lambrecht, W. R. L. Quasiparticle band structure calculation of monolayer, bilayer, and bulk MoS_2. *Phys. Rev. B* **85**, 205302 (2012).

72. Zeng, H. *et al.* Optical signature of symmetry variations and spin-valley coupling in atomically thin tungsten dichalcogenides. *Sci. Rep.* **3**, 1608 (2013).

73. Wang, H., Zhang, C. & Rana, F. Ultrafast dynamics of defect-assisted electron-hole recombination in monolayer MoS_2. *Nano Lett.* **15**, 339 (2015).

74. Cui, Q., Ceballos, F., Kumar, N. & Zhao, H. Transient absorption microscopy of monolayer and bulk WSe2. *ACS Nano* **8**, 2970 (2014).

75. Amani, M. *et al.* Near-unity photoluminescence quantum yield in MoS_2. *Science* **350**, 1065 (2015).

76. Wang, H. *et al.* Radiative lifetimes of excitons and trions in monolayers of the metal dichalcogenide MoS_2. *Phys. Rev. B* **93**, 045407 (2016).

77. Ceballos, F., Bellus, M. Z., Chiu, H.-Y. & Zhao, H. Ultrafast charge separation and indirect exciton formation in a MoS_2-$MoSe_2$ van der Waals heterostructure. *ACS Nano* **8**, 12717 (2014).

78. Rigosi, A. F., Hill, H. M., Li, Y., Chernikov, A. & Heinz, T. F. Probing interlayer

interactions in transition metal dichalcogenide heterostructures by optical spectroscopy: MoS_2/WS_2 and $MoSe_2/WSe_2$. *Nano Lett.* **15**, 5033 (2015).

79. Chen, H. *et al.* Ultrafast formation of interlayer hot excitons in atomically thin MoS_2/WS_2 heterostructures. *Nat. Commun.* **7**, 12512 (2016).

80. Shockley, W. & Read, W. T. Statistics of the recombinations of holes and electrons. *Phys. Rev.* **87**, 835 (1952).

81. Hall, R. N. Electron-hole recombination in germanium. *Phys. Rev.* **87**, 387 (1952).

82. Shi, H. *et al.* Exciton dynamics in suspended monolayer and few-layer MoS_2 2D crystals. *ACS Nano* **7**, 1072 (2013).

83. Li, L. J. *et al.* Controlling many-body states by the electric-field effect in a two-dimensional material. *Nature* **529**, 185 (2016).

84. Saito, Y. *et al.* Superconductivity protected by spin-valley locking in ion-gated MoS_2. *Nat. Phys.* **12**, 144–149 (2015).

85. Lu, J. M. *et al.* Evidence for two-dimensional Ising superconductivity in gated MoS2. *Science* **350**, 1353 (2015).

86. Lu, J. M. *et al.* Full superconducting dome of strong Ising protection in gated monolayer WS2. *Proc. Natl. Acad. Sci. U. S. A.* **115**, 3551 (2018).

87. Zhu, H. *et al.* Interfacial charge transfer circumventing momentum mismatch at two-dimensional van der Waals heterojunctions. *Nano Lett.* **17**, 3591 (2017).

88. Rivera, P. *et al.* Interlayer valley excitons in heterobilayers of transition metal dichalcogenides. *Nat. Nanotechnol.* **13**, 1004 (2018).

89. Stern, M., Garmider, V., Umansky, V. & Bar-Joseph, I. Mott transition of excitons in coupled quantum wells. *Phys. Rev. Lett.* **100**, 256402 (2008).

90. Kiršanskė, G. *et al.* Observation of the exciton Mott transition in the photoluminescence of coupled quantum wells. *Phys. Rev. B* **94**, 155438 (2016).

91. Stern, M., Umansky, V. & Bar-Joseph, I. Exciton liquid in coupled quantum wells. *Science* **343**, 55 (2014).

92. Smith, R. P. *et al.* Extraction of many-body configurations from nonlinear absorption in semiconductor quantum wells. *Phys. Rev. Lett.* **104**, 247401 (2010).

93. Chatterjee, S. *et al.* Excitonic photoluminescence in semiconductor quantum wells: plasma versus excitons. *Phys. Rev. Lett.* **92**, 67402 (2004).

94. Miller, B. *et al.* Long-lived direct and indirect interlayer excitons in van der Waals heterostructures. *Nano Lett.* **17**, 5229 (2017).

95. Meckbach, L., Stroucken, T. & Koch, S. W. Giant excitation induced bandgap renormalization in TMDC monolayers. *Appl. Phys. Lett.* **112**, 061104 (2018).

96. Steinhoff, A., Rosner, M., Jahnke, F., Wehling, T. O. & Gies, C. Influence of excited carriers on the optical and electronic properties of MoS_2. *Nano Lett.* **14**, 3743 (2014).

97. Florian, M. *et al.* The dielectric impact of layer distances on exciton and trion binding energies in van der Waals heterostructures. *Nano Lett.* **18**, 2725 (2018).

98. Kylänpää, I. & Komsa, H.-P. Binding energies of exciton complexes in transition metal dichalcogenide monolayers and effect of dielectric environment. *Phys. Rev. B* **92**, 205418 (2015).

99. Geick, R., Perry, C. H. & Rupprecht, G. Normal modes in hexagonal boron nitride. *Phys. Rev.* **146**, 543 (1966).

100. Sie, E. J. *et al.* Observation of exciton redshift-blueshift crossover in monolayer WS_2. *Nano Lett.* **17**, 4210 (2017).

101. Goodman, A. J., Willard, A. P. & Tisdale, W. A. Exciton trapping is responsible for the long apparent lifetime in acid-treated MoS_2. *Phys. Rev. B* **96**, 121404 (2017).

102. Brinkman, W. F. & Rice, T. M. Electron-hole liquids in semiconductors. *Phys. Rev. B* **7**, 1508 (1973).

103. Wang, J. *et al.* Optical generation of high carrier densities in 2D semiconductor heterobilayers. *Sci. Adv.* **5**, eaax0145 (2019).

104. Jin, C. *et al.* Imaging of pure spin-valley diffusion current in WS2-WSe2 heterostructures. *Science* **360**, 893 (2018).

105. Tran, K. *et al.* Evidence for moiré excitons in van der Waals heterostructures. *Nature* **567**, 71 (2019).

106. Jin, C. *et al.* Observation of moiré excitons in WSe_2/WS_2 heterostructure superlattices. *Nature* **567**, 76 (2019).

107. Alexeev, E. M. *et al.* Resonantly hybridized excitons in moiré superlattices in van der Waals heterostructures. *Nature* **567**, 81 (2019).

108. Asnin, V. M. & Rogachev, A. A. Mott transition in exciton system in Germanium. *JETP Lett.* **7**, 360 (1968).

109. Kaindl, R. A., Carnahan, M. A., Hägele, D., Lövenich, R. & Chemla, D. S. Ultrafast terahertz probes of transient conducting and insulating phases in an electron-hole gas. *Nature* **423**, 734 (2003).

110. Merkl, P. *et al.* Ultrafast transition between exciton phases in van der Waals heterostructures. *Nat. Mater.* **18**, 691 (2019).

111. Unuchek, D. *et al.* Valley-polarized exciton currents in a van der Waals heterostructure. *Nat. Nanotechnol.* **14**, 1104 (2019).

112. Vörös, Z., Balili, R., Snoke, D. W., Pfeiffer, L. & West, K. Long-distance diffusion of excitons in double quantum well structures. *Phys. Rev. Lett.* **94**, 226401 (2005).

113. Stern, M. *et al.* Photoluminescence ring formation in coupled quantum wells: excitonic versus ambipolar diffusion. *Phys. Rev. Lett.* **101**, 257402 (2008).

114. Costanzo, D., Jo, S., Berger, H. & Morpurgo, A. F. Gate-induced superconductivity in atomically thin MoS_2 crystals. *Nat. Nanotechnol.* **11**, 339 (2016).

115. Sanvitto, D. Observation of charge transport by negatively charged excitons. *Science* **294**, 837 (2001).

116. Munschy, G. & Stébé, B. Existence and binding energy of the excitonic ion. *Phys. status solidi* **64**, 213 (1974).

117. Raja, A. *et al.* Dielectric disorder in two-dimensional materials. *Nat. Nanotechnol.* **14**, 832 (2019).

118. O'Donnell, K. P. & Chen, X. Temperature dependence of semiconductor band gaps. *Appl. Phys. Lett.* **58**, 2924 (1991).

119. Koch, S. W., Kira, M., Khitrova, G. & Gibbs, H. M. Semiconductor excitons in new light. *Nat. Mater.* **5**, 523 (2006).

120. Butov, L. V., Gossard, A. C. & Chemla, D. S. Macroscopically ordered state in an exciton system. *Nature* **418**, 751 (2002).

121. Kulig, M. *et al.* Exciton diffusion and halo effects in monolayer semiconductors. *Phys. Rev. Lett.* **120**, 207401 (2018).